Topical Issue - Aeroacoustics: state of art and future trends

SCIENTIFIC ARTICLE

OPEN ACCESS

Cylinder aeroacoustics: experimental study of the influence of cross-section shape on spanwise coherence length

Florent Margnat[1,*], Wagner J. Gonçalves da Silva Pinto[1] , and Camille Noûs[2]

[1] Institute PPRIME, Department of Fluid Flow, Heat Transfer and Combustion, Université de Poitiers – ENSMA – CNRS, Building B17 – 6 rue Marcel Doré – TSA 41105, 86073 Poitiers cedex 9, France
[2] Cogitamus Laboratory, 6 rue Marcel Doré – TSA 41105, 86073 Poitiers cedex 9, France

Abstract – New data and review of the spanwise coherence length is provided for flows over cylinders of different cross-sections: circular of diameter d, and rectangular of sectional aspect ratios (breadth (b) to height (d) ratio AR = b/d) of 1, 2 and 3. In the present measurements, the body has both d and spanwise length of $70d$ fixed, and the Reynolds number (based on d) range 6000–27,000 is covered. Two-point data are obtained from two hot-wire probes, one fixed in the symmetry plane and the other moving on the corresponding spanwise axis. Their position in a cross plane are deduced from preliminary measurement of the mean flow with a single probe, allowing fair comparisons between the different geometries and the introduction of uncertainty bars on coherence length values. At all tested regimes, a very good agreement is noticed between velocity-based and pressure-based coherence experimental data. Coherence length definitions are revisited, and the aeroacoustically consistent, integral length definition is selected, allowing fair synthesis of literature data into a single chart and empirical functions. Definitions for coherence decay models (e.g. Gaussian or Laplacian) are also adapted so that coherence length and coherence integral shall be equivalent. This preliminary work on coherence data and its spanwise integration enables transparent regressions and model selection. Generally, the Gaussian model is relevant for the lift peak, while the coherence exhibits a Laplacian decay at harmonics. On average, at peak Strouhal number, the coherence length for the circular and square cylinders is of $5d$ while it is of the order of $15d$ for the rectangular sections. It is concluded that the flow over those latter geometries is still a two-dimensional dynamics at the tone frequency. These values are almost preserved over the tested Reynolds number range. Coherence length value at harmonics is extensively documented. Spanwise coherence length is also discussed as an ingredient of acoustic efficiency.

Keywords: Cylinder aeroacoustics, Aeolian tone, Spanwise coherence, Circular cylinder, Square cylinder, Rectangular cylinder, Coherence length

Nomenclature

AR	Sectional aspect ratio (b/d)
a	Linear regression coefficient for Gaussian model
b	Sectional breadth
d	Cylinder diameter, sectional height
f	Frequency
f_0	Lift peak frequency
f_1	Drag peak frequency
L [Λ]	Spanwise coherence length, [normalized by d]
L_G, [Λ_G]	Coherence length for Gaussian decay
L_L, [Λ_L]	Coherence length for Laplacian decay
ℓ	Cylinder wetted span
P_1–P_4	Probe locations in (x, y) plane

$\mathcal{R}$	Residual of coherence integral due to truncation
R_a^2	Adjusted determination coefficient
Re	Reynolds number, based on U_∞ and d
St	Strouhal number, based on U_∞ and d
St_p	Peak Strouhal number in Λ_I spectrum
St_m	Strouhal number of modelled coherence decay
U_∞	Upstream velocity
u_i	Fluid velocity component in the ith direction
x, y, z	Streamwise, transverse, spanwise coordinate
α	Gaussian decay coefficient ($\alpha = a^2$)
β	Regression coefficient for Laplacian model
Δz, [η]	Spanwise lag [normalized by d]
η_{lim}	Upper limit of coherence spanwise integral
η_{max}	Maximum lag included in the regression
Γ	Coherence function (normalized cross spectrum)

*Corresponding author: florent.margnat@univ-poitiers.fr

Γ_0	Threshold for definition of $\eta_{\lim}$
Γ_p, [Γ_u]	Pressure, [velocity] based coherence data
Γ_G, [Γ_L]	Gaussian, [Laplacian] coherence decay
Λ_I	Normalized, integral coherence length
θ	Peripheral angle at the circular cylinder wall

1 Introduction

1.1 Relevancy and sparsity of coherence length data

The overall goal of the present investigation [1] is the influence of shape on bluff body aeroacoustics. This mostly concerns sources of acoustical discomfort that salient parts of vehicles can be, for instance car antenna and rear mirrors, high-speed train pantographs and landing gears. Such engineering cases still faces a lack of models which could be used for low-cost diagnostics [2] at the design step. Indeed, to date, there is no aeroacoustic equivalent of head loss tables or Nusselt's number formulas to apply to typical configurations. The present paper can be viewed as a first attempt of this, through Figure 11 in particular. It focuses on experimental estimation of the spanwise coherence length in the flow over cylinders of different cross sections and at different Reynolds (Re) and Strouhal (St) numbers. This is critical to the efficient design of noise and vibration control strategies since the spanwise coherence length is one of the two major ingredients of the acoustic intensity of aeolian tones [3–6], the other one being the sectional aerodynamic force. Thus, the discrimination between shapes of rods from the aeroacoustic point of view requires the understanding of how the cross section shape influences the spanwise dynamics of the flow, which can be described in terms of coherent length.

Many of previous experimental works on spanwise topology of bluff-body flows [4, 7–12] focused on the two-point correlation. This provides an overall quantification of the spanwise organisation. The coherence function gives a better description of the dynamics through the spectral information, in particular when the flow contains peaked frequency, as it is the case for wakes in the subcritical regime. Experimental studies that reported coherence data for aeroacoustics are listed in Table 1. There have been no measurements addressing both circular and rectangular cylinders in the same campaign.

Moreover, to the best of the authors' knowledge, an experimental value for the spanwise coherent length is only mentioned in the literature for the peak frequency [5, 6, 13] and harmonics [14] and for a single configuration (the flow over a circular cylinder), yet some inconsistencies between data and reported values, as well as different definitions of the coherence length, prevent easy comparison and subsequent applications. The other aeroacoustic studies [15–17] listed in Table 1 did not report coherence length estimation. In the field of wind engineering, Matsumoto *et al.* [18] and Le *et al.* [19] reported wall pressure coherence data measured in rectangular (AR = 1 and 5, where AR is the breadth (*b*) to height (*d*) ratio) but only the (very wide)

velocity range of the wind-tunnel was given, without more precision of the tested regime. Ito *et al.* [20] reported coherence data for AR = 3.5, 5 and 8 for Re = 38,000 with grid turbulence inflow, but not for the smooth flow.

In the present study, the spanwise coherent length is estimated for a range of Strouhal number up to 0.5, for a circular cylinder, a square cylinder, and two rectangular cylinders (AR = 2, 3), for Reynolds numbers between 6,700 and 27,000. Thus, the present results provides an insight in how the Reynolds number and the shape of the body influences the spanwise coherence: they show that if the velocity does not change its value much in the tested range, the known value for the circular cylinder is not universal to other shapes. Furthermore, providing coherence length spectra allows prediction and modeling of the noise spectrum.

1.2 Coherence measurement

Another originality of the present work is to consider very large spanwise extents relatively to the height *d* (blocking dimension) of the cylinders: the open jet length is of $70d$ while the distance between the cylinder supports is of $86d$. Thus, finite length effect is minimized. Moreover, the actual coherence decay can be observed, contrary to studies listed in Table 1, which do not include measurements at spanwise lags beyond $8d$ (except Nakato's), thus reducing the observable coherence length to the same extent. In the framework of the benchmark study on the aerodynamics of a stationary rectangular cylinder with chord-to-depth ratio equal to 5 (BARC) [21], simulations has been performed up to 20 diameter long [22], however no coherence data is reported.

The spanwise distribution is here investigated by hotwire anemometer (HWA). Surface pressure measurements would be cumbersome indeed when working with different geometries because pressure taps should be installed on each test body and at fixed positions. Also, the cylinder section should be wide enough to enclose the taps, and the vortex shedding frequency could then become lower than the anechoic chamber limit if the velocity is low. On the contrary, velocity probes can be moved freely to any spanwise station and there is no limitation regarding the size and number of the obstacles, which need not to be instrumented. Geyer's investigation [17] about porous covers around the cylinder also used HWA.

The intrusive character of HWA and its incorrectness in reverse flow regions notwithstanding, one may wonder how representative of wall flow topology the HWA result is. The reviews done by Ribeiro [9] and Norberg [12] present several methods for quantifying the flow spanwise signature, and they affirm that the analysis of velocity data returns the same values as the ones obtained from surface pressure. Using both velocity and wall pressure measurements, Kacker *et al.* [8] also obtain close results, though not exactly the same, and explain the difference by turbulence induced wall pressure fluctuations that may not be seen by the velocity probes, thus generating bigger velocity correlation

Table 1. Experimental studies reporting spanwise coherence data of cylinder flows in the framework of aeroacoustics. For rectangular cross-sections (rect), the parenthesized numbers are the breadth (b) to height (d) ratio, hereafter denoted as AR $= b/d$.

Reference		Reynolds number	Cross-section	d, mm	Total span ℓ/d	Max $\Delta z/d$
Kato *et al.* (1993)	[15]	10,000	Circular	10	–	3.8
Fujita *et al.* (1998)	[23]	13,000	Rect (1.0)†	20	10	6
Nakato *et al.* (2001)	[16]	9,600	Rect (1.0,3.0)	10	180	23
Casalino & Jacob (2003)	[5]	22,000	Circular	16	18.8	5.0
Jacob *et al.* (2005)	[13]	13,000–77,000	Circular	10, 16	30, 19	6.2, 5.2
Fujita (2010)	[6]	250,000–2,000,000	Circular	297	11.2	3
Maryami *et al.* (2019)	[14]	30,000	Circular	22	20.9	6
Geyer (2020)	[17]	77,000	Circular	30	9.3	7.2
Present study		6,700–27,000	Circular	10	70	30
			Rect (1.0, 2.0, 3.0)			

† At non-zero incidence, see discussion in Appendix B.2.

lengths. This behavior is observed by El Baroudi [7] too. The effect of flow turbulence on pressure, drag and lift spanwise correlations is studied by West and Apelt [11].

1.3 Coherence length documentation

It is striking in the literature review of both experimental and numerical [24–26] works about spanwise coherence length that a new value is rarely compared to previously documented ones. Moreover, if communicated, several definitions were used, based, on one hand, on either the squared coherence or the root coherence, on the other hand, on either the lag for which a given decay is obtained (for instance, a coherence value of .5) or on the regression coefficient in a model of the decay (e.g. Gaussian decay). Finally, the regression process is never described. All of these flaws prevent a reliable use of the reported values in further applications.

In this contribution, a universal definition is attempted, based on the actual quantity that appears in the spanwise integral from Curle's formulation. That is, a definition based on coherence integral, rather than on the modelling of the decay, whom one main advantage is that it can apply to any frequency, thus providing a spectrum for coherence length, which can be directly used to predict acoustic spectra. The analytical link between the present and previous definitions is detailed. The regression is only used to refine a first estimate for the peak frequencies, and a rational process is proposed for conducting the fitting, in particular selection of the spanwise displacements which should be included in the fitting or not when the measurements include large lags.

Based on this, literature data is revisited. First, the reported values for the coherence length are converted using the present definition. Second, for studies that do not report coherence lengths, coherence data is re-analyzed in order to estimate it for the peak frequencies. Third, all of the values are compared for different geometries and regimes, so that subsequent applications can deal with uncertainties, and empirical laws are proposed. This is made visual in Figure 11, which is one of the most important in the paper.

Presented results may serve as insight for numerical simulation of such type of geometry, specially in what concerns the necessary spanwise extent for having an accurate flow. They are also of direct interest regarding acoustic prediction, where the obtained coherence lengths are parts of models of noise emission of elongated bodies [24, 27], regarding general bluff body aerodynamics for its investigation on the effect of the cross section shape [28–30], and regarding noise reduction strategies based on the destruction of flow's spanwise coherence [31].

1.4 Paper organization

The body of the paper has been divided into two main sections. First, Section 2 describes the wind tunnel facility and the experimental setup (2.1), presents the processing techniques (2.2) and the additional care taken for rectangular cylinders (2.3), in order to provide fair and reliable coherence data. Second, Section 3 deals with the coherence length definition (3.1), estimation (3.2) and results at peak frequencies and in terms of influence of shape and velocity (3.3). A link with aeroacoustic efficiency of the tested shapes is proposed in Section 3.3.4. The review of literature coherence data and coherence length estimations is pushed in Appendix B in order to lighten the main text.

2 Coherence measurement for several shapes

The measurement methodology was presented in details with first results at the Forum Acusticum (Lyon, France, 2020) [32]. Only the essentials are recalled here in order to enable understanding of the present contribution.

2.1 Experimental setup

This work was performed in the anechoic wind tunnel BETI of Institut PPRIME, at Poitiers, France. It is of closed circuit, open test section, with an exit nozzle of section 70 cm × 70 cm. Hot-wire anemometry is performed using Dantec P11 one-dimensional probes. The facility and the setup with the hot-wire probe and support are

Fig. 1. Wind tunnel facility BETI at Institut PPRIME, at Poitiers, France (left), where the cylinder and hot-wire probes are mounted (right).
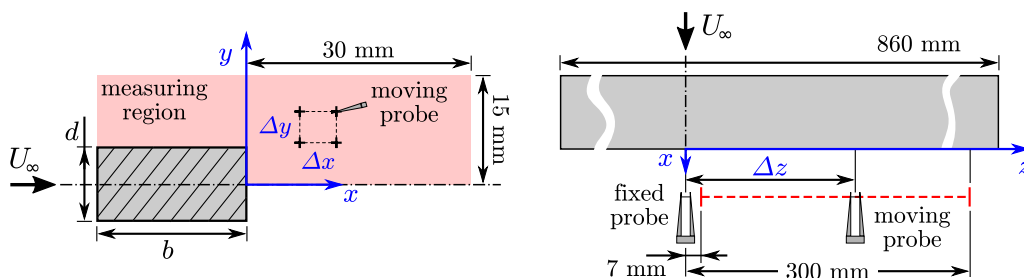
Fig. 2. Experimental setups for obtaining the mean velocity fields (left, see Sect. 2.3.1) and the spanwise coherence (right).

Table 2. Tested shapes and velocities (flow from left to right).

Shape	Circular $d = 10$ mm	Square 10×10 mm	Rectangle 10×20 mm	Rectangle 10×30 mm
U_∞ (m/s)	15, 20, 25, 30, 40	10, 20, 40	20, 40	20, 40

illustrated in Figure 1. As the coordinate system, x follows the flow direction, y is in the transverse axis and z is in the cylinders axis direction.

Tested geometries are cylinders with different cross sections (with fixed height of $d = 10$ mm): circular cylinder; square cylinder; rectangular cylinder of dimension $d \times b = 10 \times 20$ mm^2; and rectangular section of dimension $d \times b = 10 \times 30$ mm^2. The aspect ratios AR $= b/d$ (see Fig. 2, left) are thus of 1, 2 and 3, respectively. No end plates are used, for that technique of flow confinement modifies the acoustic radiation [33]. The cylinders extend beyond the shear layers, so that the actual wetted length is about that of the jet, $\ell \approx 70d$, with uncertainties due to the mixing layers. This very large span reduces end-effects.

At a given flow velocity U_∞, the Reynolds number Re based on it and d is the same for all geometries. Similarly, d is used as reference for the Strouhal number St $= fd/U_\infty$, where f is the frequency. Tested velocities, indicated in Table 2 for each shape, range from 10 m/s to 40 m/s, leading to $6,700 \leq$ Re $\leq 27,000$ for airflows at about 20 °C.

For performing coherence and correlation calculations, a fixed hot-wire probe is simultaneously recording the velocity magnitude at the cross symmetry plane of the cylinder ($z = 0$ mm), while the same quantity is measured by the moving probe in the spanwise direction at fixed XY coordinates (see Fig. 2, right). Due to the supports of the hot-wires, the starting point of the moving probe is at a spanwise distance of $\Delta z = 0.7d = 7$ mm from the fixed probe. A total of 48 spanwise positions are used, up to $z = 300$ mm. Sampling frequency and time of 6.4 kHz and 30 s are selected, respectively.

2.2 Coherence spectrum estimation and validation

At each spanwise location, the power spectral density is computed using Welch estimator. To harmonise the uncertainty on peak Strouhal number for different velocities while the recording time is the same, a constant Strouhal number resolution is specified to ΔSt $= 0.001$ (instead of constant segment size). Also, a Chebyshev window is used,
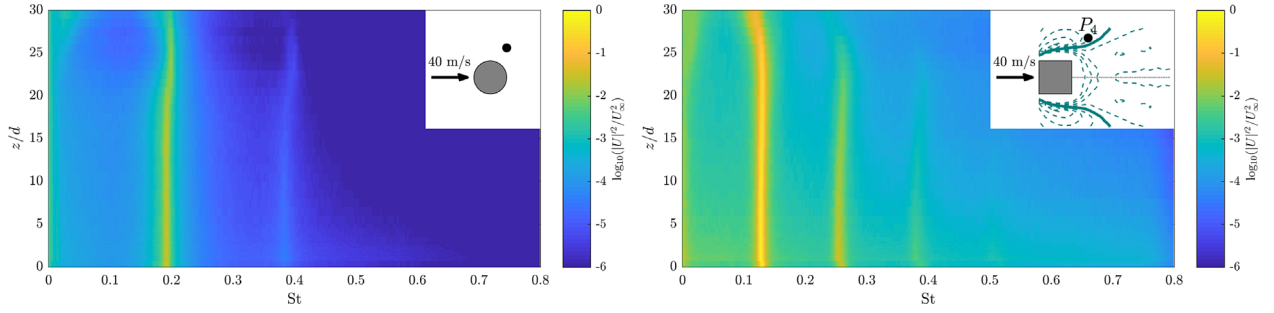
Fig. 3. Spanwise distribution of the velocity power spectral density for the flow over the circular (left) and square (right) cylinders, at Re = 27,000. Inset is the case. The black bullet (•) indicates the probe position and the lines are mean flow velocity contours (see Sect. 2.3.1).

with 50% overlap and the segment size is doubled by zero padding. This post-processing leads to an *a priori*, absolute uncertainty of ±0.0005 on the values of peak Strouhal number reported herein.

Spanwise maps of the velocity fluctuation frequency content are shown in Figure 3 for the circular and square sections at $U_\infty = 40$ m/s. The spanwise homogeneity is good up to 20 diameters away from the jet center for the main peak, in terms of spectrum level at the peak. Its extent is shorter for harmonics, however. The side effect leads to a peak Strouhal number slightly higher than at the central region for the circular section, while it is decreased for the square section. Maps for other velocities, geometries and measurement points are given in [1]. It is concluded that the flow is statistically homogeneous in z for such set-up and models, to a sufficient degree enabling spanwise coherence analysis.

The velocity spanwise coherence Γ_u is defined as the normalized, cross spectrum of two HWA fluctuation signals $\tilde{u}_i(t)$ and $\tilde{u}_j(t)$ recorded at two spanwise positions, noted z_i and z_j respectively. It is a function of the frequency and of the position (x, y) in the transverse plane, and, assuming spanwise homogeneity, an even function of the spanwise lag $\Delta z = |z_i - z_j|$. One then has:

$$\Gamma_u(\eta, f) = \frac{\left| u_i u_j^* \right|}{\sqrt{u_i^2} \sqrt{u_j^2}}, \qquad (1)$$

where $\eta = \Delta z/d$, u_i is the (auto)spectrum of $\tilde{u}_i(t)$, and the superscript * indicates the complex conjugate, while $|\cdot|$ is the modulus. The coherence calculations are based on averaged spectral density, using the same settings as for the velocity spectra calculation. Should the term *magnitude squared coherence* be used, this corresponds to Γ_u^2. The coherence value for $\eta = 0$ (the test of the signal with itself) is unitary by construction.

Whether velocity coherence is equivalent to wall-pressure based coherence Γ_p is assessed in Figure 4. Coherence data is plotted as a function of the spanwise lag at the main peak frequency, namely, the lift fluctuation at the shear-layer flapping frequency.

For the circular cylinder flow, Figure 4 (left), present data for $U_\infty = 40$ m/s is compared to four data-sets from

the literature, all obtained by wall-pressure measurements, in the same Reynolds number range. The collapse of the data for the short lags (namely $\eta \leq 2$) is noteworthy. For larger distance between the sensors, there is more dispersion among the data-sets, and the coherence decay for a given data-set is less regular. In the range $2.5 \leq \eta \leq 5$, velocity coherence is slightly lower than wall pressure coherence. This could be associated with probe intrusion or with higher turbulence level in the shear-flow than at the wall.

For the square cylinder flow, Nakato *et al.* [16] reported three points for $\Gamma(\eta)$ at the peak frequency, from velocity measurements one height downstream of the body. That for $\eta = 5$, the shortest documented one, is in perfect agreement with present data as visible in Figure 4 (right). The two other points are for larger lags, where coherence level becomes similar to measurement noise, which can be quantified as up to ≈ 0.2 in the present case (see coherence maps in Fig. 6 for instance). Nevertheless, both data-sets exhibit consistent decays. For the shortest lags, present coherence does not exceed 0.85. This kind of saturation could be due to probe interference, reinforced by a loss of accuracy of the HWA here in the near wake, reverse flow region.

Further comparisons are proposed in Appendix B and Figure B.2, at other regimes for the circular cylinder, and for rectangular cylinder of AR = 3 with data of Nakato *et al.* [16] too and with numerical data reported by Rakugou *et al.* [26]. Recall that, to the best of our knowledge, direct comparisons of coherence data such those in Figures 4 and B.2, have not been conducted before. For the sake of completeness, comparison with literature data for spanwise correlation is extensively conducted in [1]. The conclusion of this section is that the present measurements generates spanwise coherence data in agreement with literature.

2.3 Rectangular cylinders specific issues

The present paper does not aim only to enrich the literature with spanwise coherence length values for *a given*, less documented, shape, e.g. the square section cylinder, but also to provide fair comparison *between* shapes, from an aeroacoustic design point of view. Ribeiro [9] indicates that spanwise correlation is relatively independent from the measuring location in the XY plane provided it is above
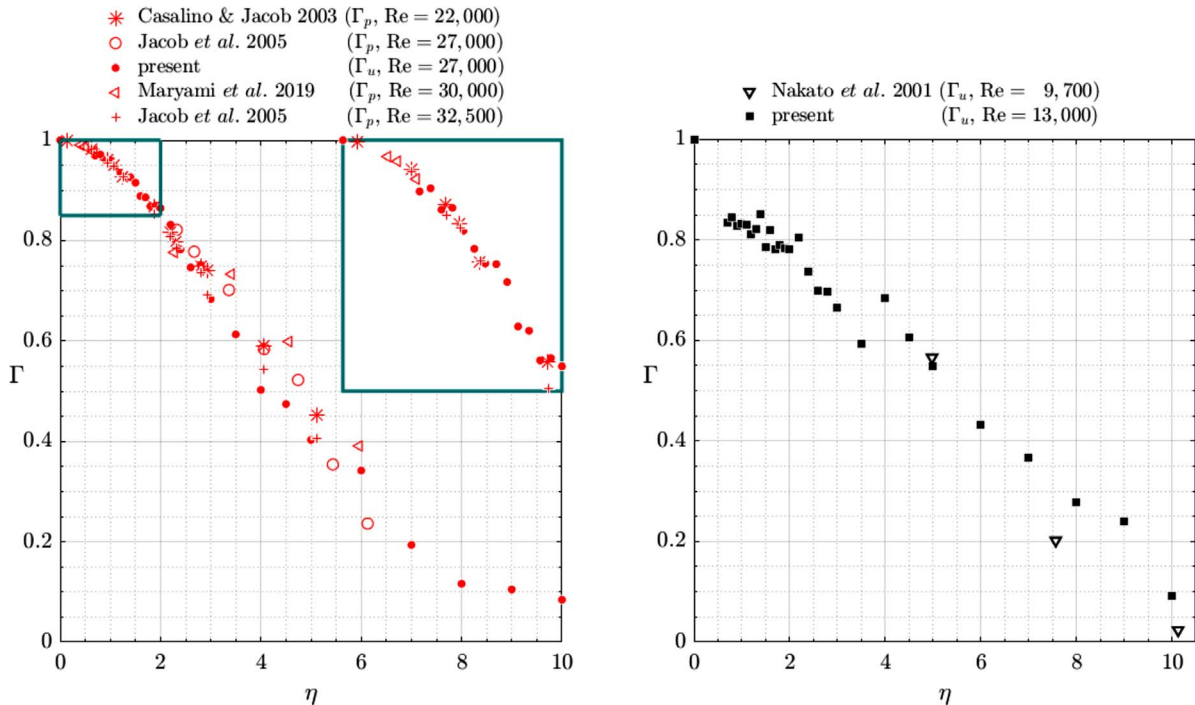
Fig. 4. Spanwise coherence data in the flow over the circular (left, probe at $(x, y) = (0, 0.9d)$ for present data) and square (right, probe at $(x, y) = (1.0d, 0)$ for both data-sets) cylinders, at the main peak frequency (St = 0.193 and 0.125 for present data on left and right, respectively).

the mixing layer and at a reasonable downstream location to capture more than just the inlet flow. That is how the position $(0, 0.9d)$ has been selected for coherence measurement in the flow over the circular cylinder. For the rectangular cylinder, a two-step measurement method is set up, in order to ensure that the hot-wire placement does not bias the coherence length estimation.

2.3.1 Mean flow scan

Positions where the spanwise study shall be conducted afterwards are based on a preliminary map of the mean, homogeneous, velocity magnitude in the transverse (XY) plane using the moving-probe, as depicted in Figure 2 (left) and described in details in [32].

Mean flow topology for the rectangular cylinders at 20 and 40 m/s are shown in Figure 5 through isocontours of the velocity norm, and by underlining the unitary contour, where $U = U_\infty$, hereafter referred to as the reference line. For each case, the latter starts close to the upstream edge, then deviates from the wall to a plateau, and then deviates again upward. Due to use of HWA, the recirculation region can not be visualised. However, the contours allow to relativise its length between the geometries and the velocities. Moreover, reattachment before the downstream edge can be guessed for AR = 3.

Given this universal evolution of that meanflow topology, in particular the reference line, four typical points are selected: P_1 is located at $(1.0d, 0)$ and serves for reference; P_2 is the closest to the upstream edge, at the point

of maximum velocity norm; P_3 is taken 2–3 mm above the reference line plateau; and P_4 2–3 mm above its maximum curvature. Thus, the probe is not at the same absolute position in the XY plane for all of the cases (except for P_1) but it is at topologically equivalent position from the mean flow point of view. P_1 is not used for AR > 1 because at this location, unsteady reverse flow is expected, meaning that HWA may not be reliable. Also, in order to lighten the measurements, P_3 is only included for the square cylinder due to its intermediary location between P_2 and P_4. The probe location for each case is given in Appendix A (Tab. A.1) and its influence on the spanwise coherence map is described in the next section.

2.3.2 Influence of probe position

Maps of Γ_u (St, η) are drawn in Figure 6 for the square cylinder flow at 20 m/s, for the four probe locations. Note that the four plots do not come from simultaneously recorded data: the flow perturbation due to the probe is different for each position, and for each lag. At the main peak frequency St = 0.125, the coherence decay is very similar between the four probe positions: the coherence peak emerges from the background up to $\eta \approx 8$, except for P_4 where this ends around $\eta \approx 6$. This is also noticed for the drag harmonic at St = 0.250, with emergence up to $\eta \approx 3.5$, a little bit less for P_1. The third and fourth peaks (St = 0.375 and 0.500, respectively) emerge differently depending on the probe location. Similar observations are made for the two other velocities considered for the square
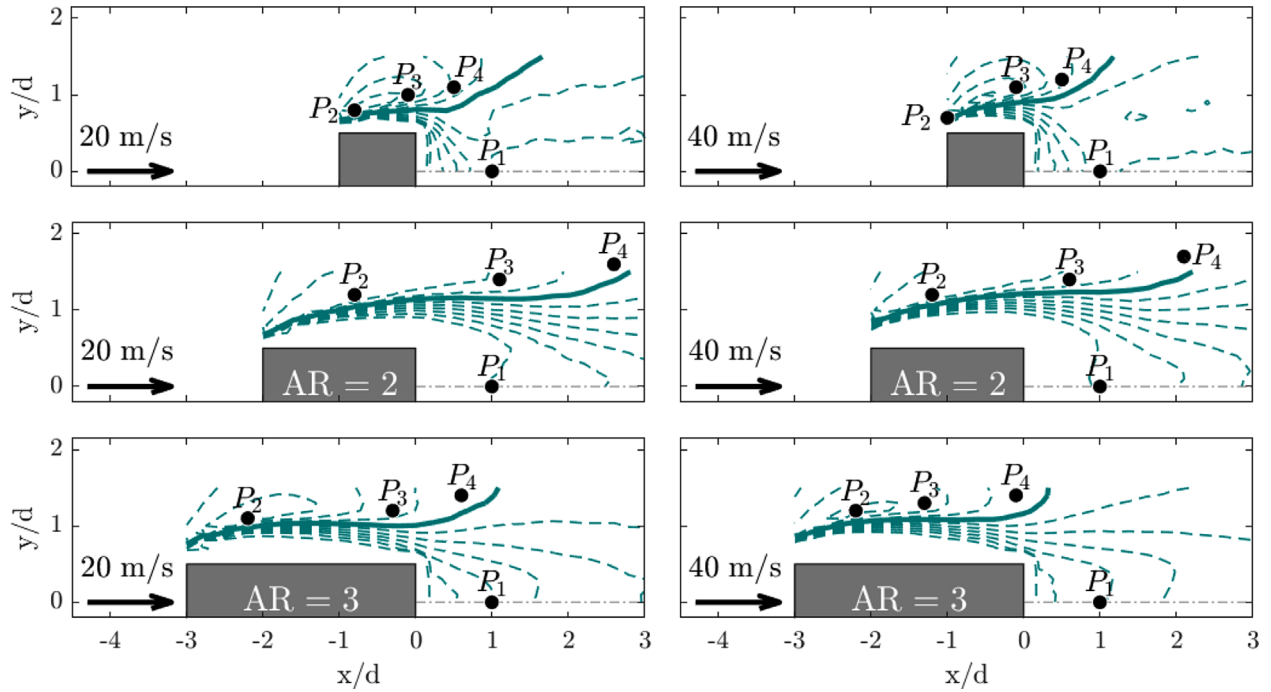
Fig. 5. Mean flow over a rectangular cylinder of AR = 1 (square cylinder, top), 2 (middle) and 3 (bottom) at Re = 13,000 (left) and Re = 27,000 (right). Isocontours of velocity norm from 0.4 U_∞ to 1.6 U_∞ by step of 0.1 U_∞. The full, thick line is where $U = U_\infty$. The labelled bullets (•) are the position of the probes in the spanwise study. The case AR = 1, U_∞ = 10 m/s is shown in Figure A.1.
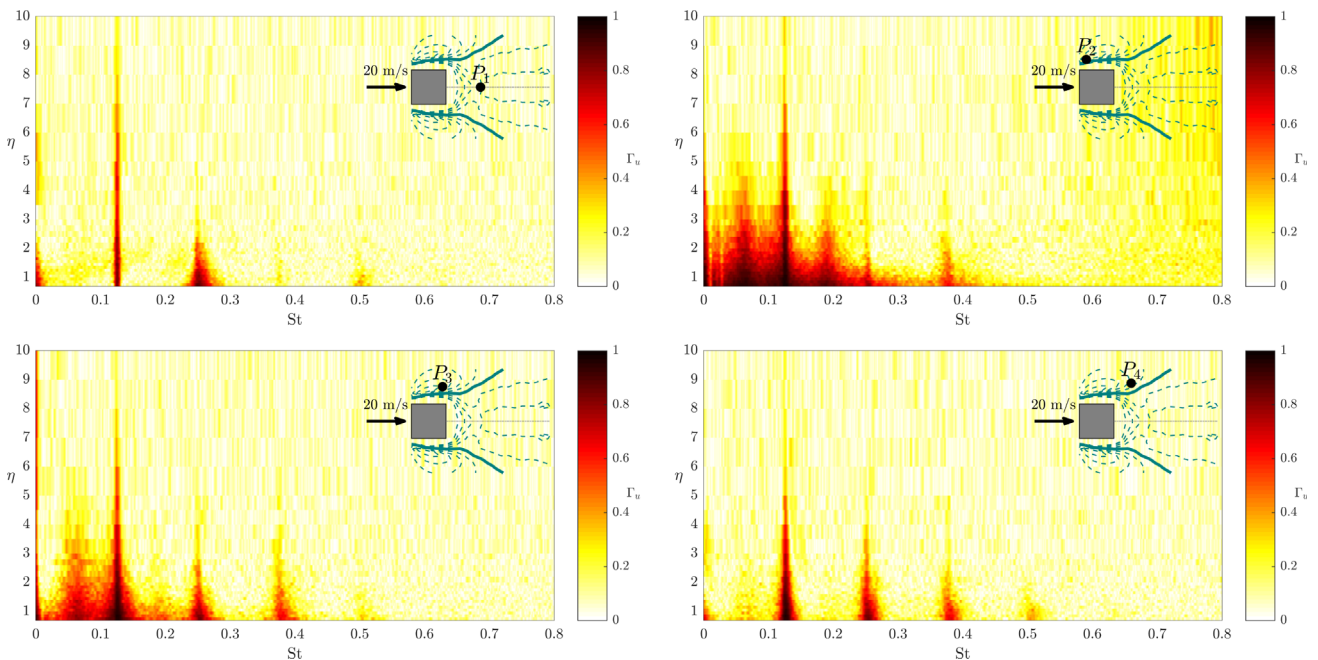
Fig. 6. Spanwise coherence of the velocity (Γ_u) in the flow over the square cylinder, at Re = 13,000. Inset, the black bullet (•) indicates the probe position and the lines are mean flow velocity contours (with same legend as Fig. 5).

cylinder (10 and 40 m/s [32]) and between P_2 and P_4 for the other rectangular cylinders [1].

The map for P_1 exhibits a sharper lift peak, and almost no emergence at its third multiple. This is consistent with the probe location downstream the body, where the wake

global oscillation [34] imprint on the probe may be less perturbed by inflow turbulence or shear-layer instabilities. At the same time, that region is where the vortices are generated and shed, associated with base pressure fluctuation at twice the shear-layer flapping frequency. The maps

for P_2 and P_3 shows similar regions of significant coherence between the peaks. Rokugou *et al.* [26] also reported significant level of coherence ($\Gamma \approx 0.5$ for $\eta \approx 1$) for St = 0.06 in the flow over a rectangular cylinder of AR = 0.6. Or this may be due to the less distance of these positions to the wall, leading to a likely influence of the hot-wire on the local flow dynamics.

2.4 Conclusion on the methodology

The present protocol of spanwise coherence measurement using HWA in wind tunnel has been assessed by comparison to literature data and by the use of a couple of probe positions based on the mean flow topology. Besides the validation of the setup, this allows an estimate of uncertainties on the coherence length, as presented in the next section. For rectangular cylinders at the main flow frequency, the spanwise coherence distribution appears almost independent of the probe position. Its measurement using HWA can thus be considered as representative of that of the lift.

In the remaining part of this paper, the quantity Γ_u, defined in equation (1) and obtained for a given case (shape, velocity, probe position) from the processing of HWA signals described in this section, refers to as *the data*.

3 Coherence modelling and coherence length

3.1 An aeroacoustically consistent definition

The spanwise coherence length emerges from the derivation of the expression of the acoustic intensity spectrum, in the case of the noise generated aerodynamically by the flow over a cylinder. At low Mach number, the cross section is acoustically compact, and the integration of Curle's surface source must include phase lag in the spanwise direction only. Given the close relationship between coherence length and spanwise Curle's integration, the spanwise coherence length L shall be defined as an integral length:

$$\frac{L(f)}{d} = \Lambda(f) = \frac{1}{2} \int_{-(\ell/d)/2}^{(\ell/d)/2} \Gamma(\eta, f) \mathrm{d}\eta, \qquad (2)$$

where Λ is the spanwise coherence length normalized by the cylinder height. Such definition, which is mentioned in [14, 16, 35], is the frequency domain equivalent of the spanwise correlation length or scale defined in the time domain [3, 36]. Besides its formal link with Curle's approach, it is also closer to *the data* than definitions based on a modeling of the coherence decay as Gaussian or Laplacian, which requires regression (see Sect. 3.3). Moreover, such theoretical decays do not fit *the data* for some cases at some frequencies. Finally, (2) does not rely on any arbitrary setting of coherence decay, which may also confuse the users, given that the median value of 0.5 is specified for Γ by Kato *et al.* [15] and Orselli *et al.* [25], while Maryami *et al.* [14] set it for Γ^2. Halving the two-sided integral is the only

addition of present definition to Curle's integral. It is nevertheless introduced here as a concession in order not to go too off usually known values for the circular cylinder flow. The direct estimation of L from (2) is not free from practical difficulties, however. A mix of three methods deduced from the three types of definition (data quadrature over spanwise lags, lag for a given coherence level, and regression with a decay model) has been found useful to rationalize the estimation of the coherence length.

3.2 Frequency dependent coherence length

3.2.1 Two methods of estimation

Assuming that the coherence is an even function of the lag, (2) can be evaluated using a trapezoidal rule over the spanwise range of the moving probe. However, in order that the quadrature to be not biased by measurement noise for large lags, the upper bound is adjusted for each frequency. Namely:

$$\Lambda_I(f) = \int_0^{\eta_{\lim}(f)} \Gamma(\eta, f) \mathrm{d}\eta, \qquad (3)$$

where Λ_I stands for the quadrature estimation of Λ, and $\eta_{\lim}$ is the smallest element of the first set of three straight lags returning $\Gamma < \Gamma_0 = 0.2$, at a given frequency. This truncation is mainly useful between the peak frequencies, where significant level of coherence is noticed for a small portion of the span only (see Fig. 6): the signal to noise ratio is then very weak when including all of the measured lags. By truncating this, it is likely that Λ_I systematically underestimates Λ. Nevertheless, this error can be quantified, by modeling the coherence decay. A Gaussian decay corresponds to:

$$\Gamma_{\mathrm{G}}(\eta) = e^{-\alpha\eta^2}, \qquad (4)$$

where Γ_{G} is the Gaussian model of the coherence Γ and the frequency dependence of α has been omitted for conciseness. Assuming that the coherence is vanishing at the cylinder ends, that is $L \ll \ell$, leads to the Gaussian coherence length

$$\Lambda_{\mathrm{G}} = \int_0^{\frac{\ell}{2d}} \Gamma_{\mathrm{G}}(\eta) \mathrm{d}\eta \approx \int_0^{+\infty} e^{-\alpha\eta^2} \mathrm{d}\eta = \frac{1}{2}\sqrt{\frac{\pi}{\alpha}} \qquad (5)$$
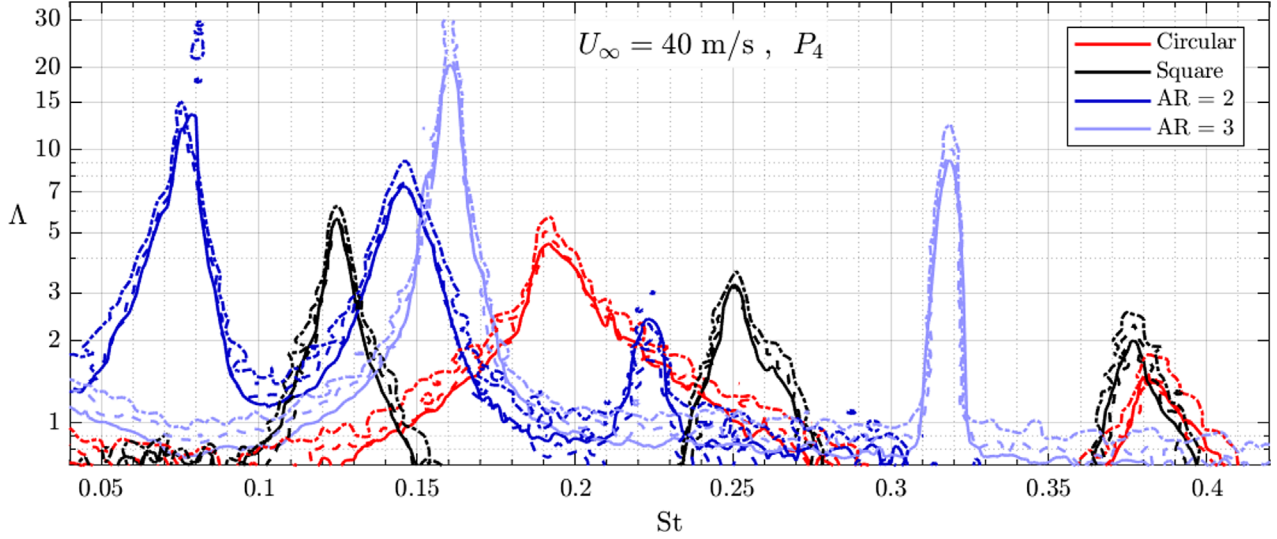
meaning that

$$\Gamma_{\mathrm{G}}(\eta) = e^{-\pi\left(\frac{\eta}{2\Lambda_{\mathrm{G}}}\right)^2}. \qquad (6)$$

The integral length is thus commonly referred to as the Gaussian half-length. The lag for which the coherence falls to Γ_0 is thus given by

$$\eta_{\lim} = 2\Lambda_{\mathrm{G}}\sqrt{\frac{-\log\Gamma_0}{\pi}} \approx 1.43\Lambda_{\mathrm{G}}, \qquad (7)$$

where log is the natural logarithm. The residual of the truncated integral is then [37]:

Fig. 7. Frequency dependent, normalized spanwise coherence length in the flow over cylinders, at Re = 27,000. Measurements at P_4 for rectangles (see Sect. 2.3.1). Full lines: estimation from spanwise integration of coherence data (3); dashed and dash-dotted lines show isocontours of $\Gamma_u = \exp(-\pi/4)$ and $\Gamma_u = \exp(-1)$, respectively, in the (η, St) field, corresponding to a coherence decay assumed as either Gaussian or Laplacian, respectively.

$$\mathcal{R} = \Lambda - \Lambda_I = \int_{\eta_{\lim}}^{+\infty} e^{-\pi\left(\frac{\eta}{2\Lambda_G}\right)^2} \mathrm{d}\eta,$$

$$= \Lambda_G\left[\mathrm{erf}\left(\frac{\sqrt{\pi}}{4}\frac{\ell}{L}\right) - \mathrm{erf}\left(\sqrt{-\log\Gamma_0}\right)\right]. \quad (8)$$

The first term in the brackets is greater than 0.9999 as soon as $\ell \geq 6.1L$. Since the second is 0.9272, the conclusion is that $\mathcal{R} \approx 0.1\Lambda_G$. Modeling the coherence decay with a Laplacian function, namely:

$$\Gamma_L(\eta) = e^{-\frac{|\eta|}{\Lambda_L}} \quad (9)$$

leads similarly to $\eta_{\lim} = -\Lambda_L \log\Gamma_0 \approx 1.61\Lambda_L$ and a residual about $0.2\Lambda_L$.

A coherence decay model can also be exploited to estimate the coherence length from the lag at which the coherence falls on a given value. Indeed, at $\eta = \Lambda_G$, one has $\Gamma_G = \exp(-\pi/4) \approx 0.46$. Similarly, Γ_L ($\eta = \Lambda_L$) = $e^{-1} \approx 0.37$. Consequently, plotting the corresponding isocontours of *the data* in the (η, St) field yields two other evaluations of the coherence length spectrum.

The three results are plotted in Figure 7 for the four geometries at $U_\infty = 40$ m/s and for probe at P_4. Before the trends are described in the next section, the spectra are discussed here from the point of view of methodology. The agreement between the two methods (quadrature and isocontours) is noteworthy. Particularly at the peaks, Λ_I can hardly be distinguished from the isocontour that assumes a Gaussian decay. The one that assumes a Laplacian decay returns slightly higher coherence estimation. This is expected since it is a lower value of Γ within the same *data*. Note also that the contour plot resolution

corresponds to that of the measured lags, which is of $1d$ for $\Delta z \geq 5d$. The results for $U_\infty = 20$ m/s and for the probes at P_2 are shown in the Supplementary file.

Recall that the evaluation of Λ_I does not require any decay model, thus it can be considered as a good way to compress *the data*. However, it requires a good lag resolution and that large lags are included in the measurement span such that the coherence is small enough at the end of the integration domain. If it is not, then Λ can still be evaluated from Λ_I by integrating Γ^2 instead of Γ. This reduces the lag where the coherence vanishes and the background noise in the coherence map at the same time. However, the conversion of the resulting integral into Λ_I requires a decay model, noting that:

$$\int_0^{+\infty} \Gamma_G^2 \mathrm{d}\eta = \int_0^{+\infty} e^{-2\alpha\eta^2}\mathrm{d}\eta = \frac{1}{2}\sqrt{\frac{\pi}{2\alpha}} = \frac{1}{\sqrt{2}}\int_0^{+\infty} \Gamma_G \mathrm{d}\eta,$$

while $\int_0^{+\infty} \Gamma_L^2 \mathrm{d}\eta = \frac{1}{2}\int_0^{+\infty} \Gamma_L \mathrm{d}\eta.$

From the fact that the contour based on the Laplacian decay is generally higher than Λ_I, it could be concluded that the Gaussian decay models *the data* better, however this is investigated further in Section 3.3.2.

3.2.2 Influence of shape and velocity

The above described approximations notwithstanding, Figure 7 provides direct visualizations of the influence of cross-section shape on the spanwise coherence length spectrum in cylinder flows, that is, in Curle's formulation framework, of their aeroacoustic efficiency. To estimate the far-field noise spectrum, this should be multiplied by the source amplitude, as given by the sectional force spectrum, whose estimation [12, 38] is outside the scope of the present contribution. The geometry influences not only
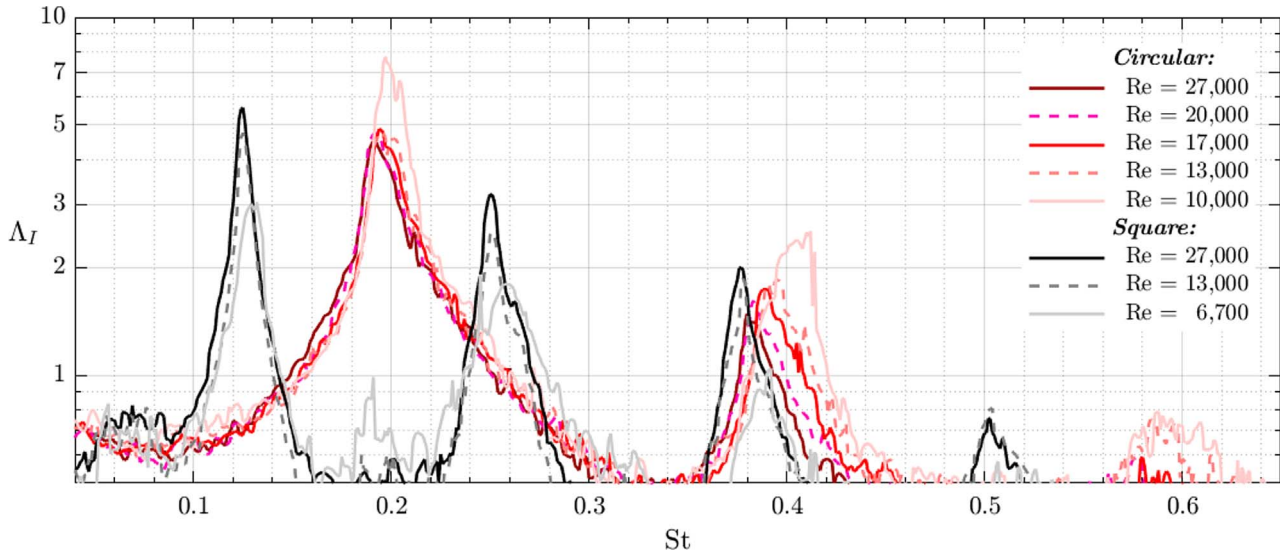
Fig. 8. Frequency dependent, normalized spanwise coherence length in the flow over circular and square cylinders, estimated from integration of coherence data (3). Measurements at P_4 for the square section. Results at other probe locations are available in the Supplementary file.

the coherence length value at peak frequencies, but also the shape of the full spectrum, in terms of peak width and harmonics. With the present definition (2), one obtains $L \approx 5d$ for the circular cylinder at the main peak St = 0.19, and $\approx 2d$ at the first harmonic. The value is slightly higher for the square cylinder, with $L \approx 6d$ for St = 0.125, $\approx 3d$ at 0.25, and as significant at the third peak St = 0.375 as at the drag peak for the circular section. One of the main results of the paper is the very high coherence length values measured for rectangular cylinders AR = 2 and AR = 3: around $15 - 20d$ for the first peak, and $7 - 10d$ for the second, depending on velocity and probe location. Note that for AR = 2, the two first peaks (St = 0.08 and 0.14) are not harmonic.

A continuous sharpening of the main peak is noticed when moving from the circular to the square section then increasing aspect ratio of rectangular section. At Re = 27,000, the circular section also leads to a peak base, that is an increasing significant coherence length for $0.15 \leq \text{St} \leq 0.18$ and the equivalent hillside for $0.22 \leq \text{St} \leq 0.26$. Such base is also visible, while sharper, for the square and AR = 2 rectangle. For both its lift and drag frequencies, the coherence length spectrum of the flow over the AR = 3 rectangle remains highly tonal. Combined with the coherence length value that reaches nearly the whole (half-)span of the jet core, the peak sharpness for this geometry leads to the conclusion that this bluff-body flow is still mostly dominated by a two-dimensional dynamics at this regime.

The influence of velocity is illustrated in Figure 8, which includes all of the regimes tested in the present experiment for the circular and square sections. For both sections, the coherence length spectrum is singular at the lowest velocity, however in an opposite sense: for the circular cylinder, the coherence length at peaks is higher at Re = 10,000 than for faster flows, while for the square cylinder, it is lower at

$U_\infty = 10$ m/s than at 20 or 40. This may be attributed to different transition to turbulence scenario for different shapes and flow modes. However, for the circular cylinder, the spectra appear very similar for the four other tested velocities, meaning that the flow may have reached an established (Reynolds number) regime, yet this is not so obvious for the drag peak. Figure 8 also reveals significant coherence length values at the harmonics, which received few treatment in literature although they may generate loud tones. This is critical for the square section in particular. That is why the coherence length at the harmonics is included in the tabulation of present data (see Supplementary file), and its estimation accuracy is improved by feeding a regression procedure with the present section basic estimations, as described in the following.

3.3 Coherence length at peak frequencies

This final section is devoted to a refined estimation and a discussion of spanwise coherence length at peak frequencies. The estimation uses a linear regression procedure with either a Gaussian or a Laplacian coherence decay model. Before presenting it, the peak frequency shall be defined.

3.3.1 Peak Strouhal number characterisation

A first guess of the Strouhal number that leads to a coherence length peak is obtained from local maxima in Λ_I spectra (e.g. Fig. 7). The maximum seeking procedure is automated, but for harmonics, whether it is an effective peak (emerging from noise), or a bias from spectrum variance, is manually checked for each case. This yields 2, 3 or 4 peaks for a given case, and a total of 75 peaks including all of the 25 cases (shape, velocity, probe location). These are documented in a Supplementary file, in terms of peak location noted St_p and value, that is $\Lambda_I(\text{St}_p)$.
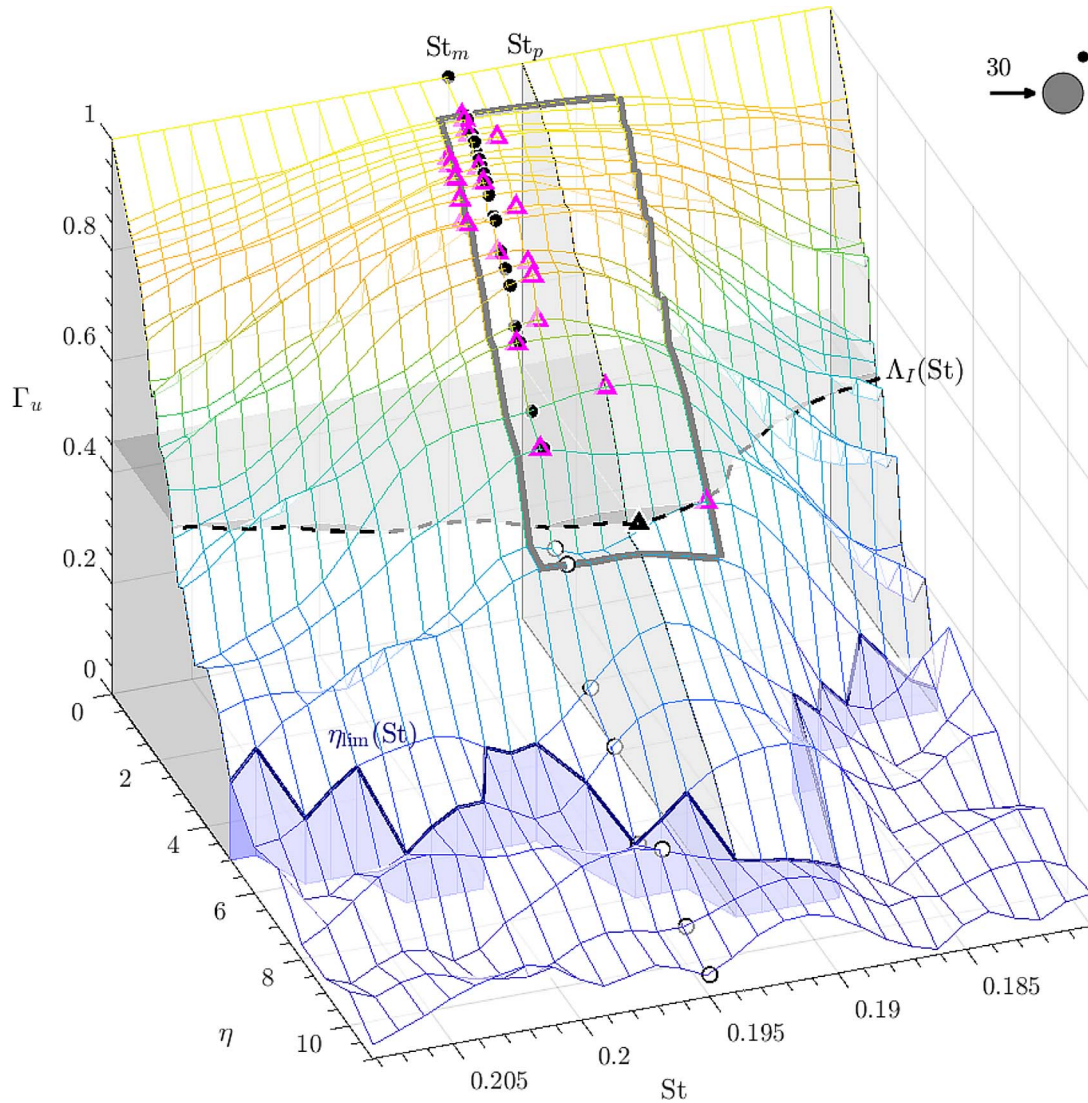
Fig. 9. Surface plot of coherence data $\Gamma_u(\eta, \mathrm{St})$ illustrating the nomenclature and methodology for the estimation of St_p and its bounding. Dashed line: integral coherence length Λ_I at a given Strouhal number; blue line and panels: $\eta_{\lim}$, limit of quadrature evaluation indicated by the vertical grayed areas; filled triangle (▲): peak of coherence length at St_p; open triangles (△): maxima of coherence at a given lag; thick grey lines: Strouhal number uncertainty range around St_p; filled circles (●): lags below $\eta_{\max} = \Lambda_I$ used for model fit at St_m; open circles (○): $\eta > \eta_{\max}$. Data for the circular cylinder flow at Re = 20,000.

However, for a given case and peak, the Strouhal number bin corresponding to a local maximum in the coherence spectrum is not necessarily the same for all lags, as illustrated in Figure 9, because of measurements and processing bias. The integral coherence length $\Lambda_I(\mathrm{St})$ (horizontal, grey area) is close to the isocontour $\Gamma = \exp(-\pi/4) \approx 0.46$, see Section 3.2.1 and Figure 7. The local maxima of coherence at a given lag (△) are collected for $\eta \leq \Lambda_I(\mathrm{St}_p)$ (thick grey lines at $\eta =$ constant) to build the Strouhal number uncertainty range around St_p that is tabulated for each peak in the Supplementary file (thick grey lines at $\mathrm{St} =$ constant). Within this range, a Gaussian decay fits *the data* correctly below $\eta_{\max} = \Lambda_I$ (●) and the maximum coherence length is obtained at St_m, while the data for $\eta > \eta_{\max}$ (○) undergoes excess of coherence that leads to excess of Λ_I and a biased $\mathrm{St}_p \neq \mathrm{St}_m$ for that case, see Section 3.3.2 and Figure 10. That

Strouhal number interval is provided in addition to St_p to handle such uncertainty and enable fair comparisons with other authors. Note that to ensure the local maximum in the coherence spectrum at a given lag are avatars of the same peak indeed, the peak seeking is restricted to $\mathrm{St}_p \pm 0.03$, that is ± 30 bins around the St_p (recall that the non-dimensionalized frequency resolution has been set as 0.001 for all velocities, see Sect. 2.2), and to lags less than or equal to $\Lambda_I(\mathrm{St}_p)$ to ensure emergence from coherence residuals.

In more than 90% of the peaks, St_p belongs to that interval. For the 7 exceptions (out of the 75 peaks), this means that no local maximum was found in the coherence spectrum at this frequency at any lag, and that a significant contribution to the integral is brought by larger lags than Λ_I. This could be a side-effect through the denominator
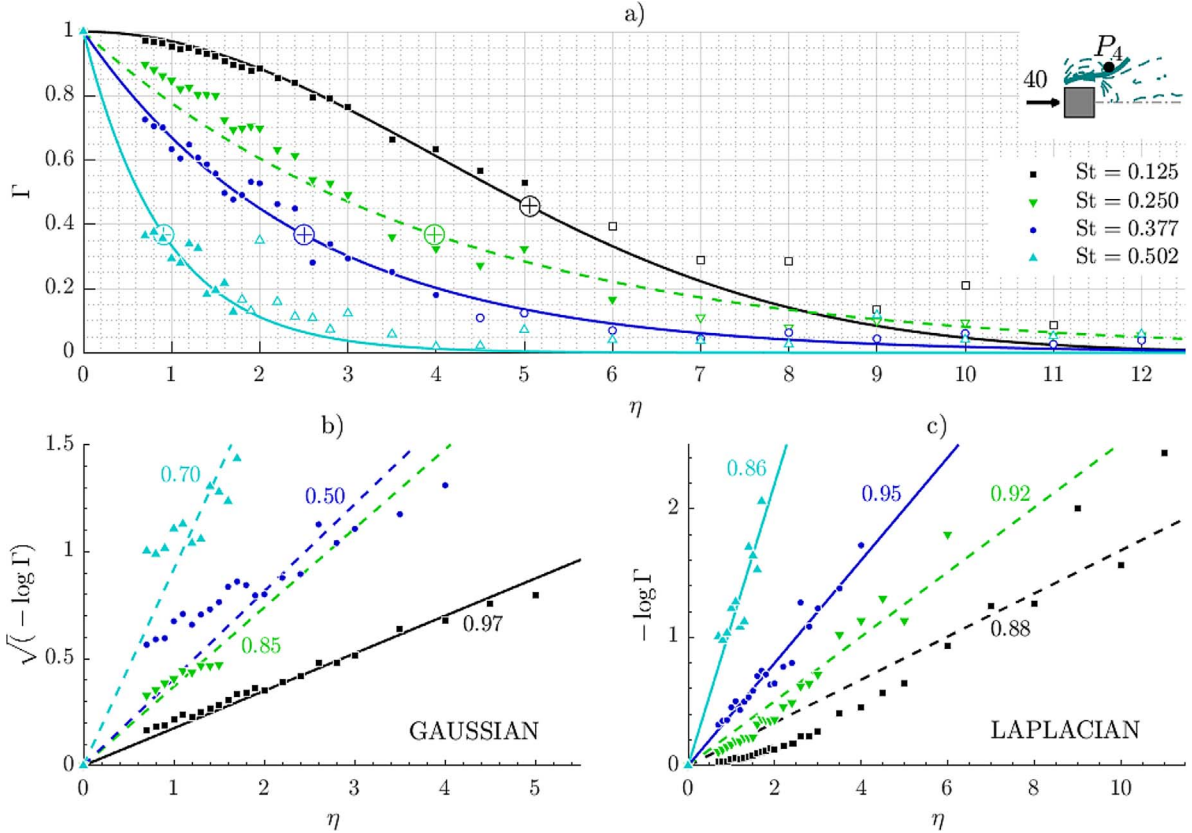
Fig. 10. Estimation of coherence length at peak frequencies for the square cylinder flow at $Re = 27{,}000$ with probe at P_4: coherence data (symbols) fitted with decay model (lines). Single parameter, linear regressions are applied to a data excerpt (full symbols) for a Gaussian (b) and a Laplacian (c) decay. In (b) and (c), the numbered label next to each line is the adjusted determination coefficient R_a^2 of the corresponding regression. The line is full or dashed whether the model is selected or not, respectively. Data for $\eta > \eta_{max}$, excluded from the regression, is plotted in (a) for illustrative purpose (open symbols). The refined coherence length values can be read on the lag axis where Γ reaches the appropriate value for the selected model ($\oplus$).

in (1): on one hand, for large z, a peak in the velocity spectra can shift and/or spread (see Fig. 3), resulting in significant energy at frequencies wide of the peak identified at smaller z; on the other hand, depending on geometry, velocity, measurement point and peak, the level of $\sqrt{u_i^2}$ does not sustain up to the same z. For low velocity and/or large coherence length, its decay may start before the coherence has decayed to Γ_0. Relatively to shorter lags, the autospectrum of the moving probe becomes smaller, resulting in an excess of coherence for $\Lambda_I \leq \eta \leq \eta_{lim}$. To the best of our knowledge, such phenomenon has not been reported in literature, because it concerns coherence estimation at large lags (see Tab. 1).

However, the interval in general, and the gap between St_p and the interval for those exceptions, is a couple of bins only, while the worst exception is for the circular cylinder drag peak at $U_\infty = 15$ m/s: $St_p = 0.412(0.392 - 0.405)$, which corresponds to a 5% relative uncertainty in the peak Strouhal number estimation.

3.3.2 Peak coherence length estimation

Like for St_p, a first guess of Λ at tone frequencies is obtained from the value of the integral length at this peak

Strouhal number, that is $\Lambda_I(St_p)$. Although this is the most faithful to *the data*, the numerical estimation of Λ_I can be biased for the aforementioned reasons (spanwise inhomogeneity, lag resolution and trapezoidal method, truncation at η_{lim}). But if *the data* were correctly described by a model, then the coherence length yielded by the model would be free from some of the experimental and computational bias. Moreover, modeling the coherence field $\Gamma(\eta, St)$ could be very useful for subsequent applications, for instance flow as a source of sound radiated to a wall-bounded environment, such as installation effects [39].

That is why the data $\Gamma_u(\eta, St)$ is fitted with a Gaussian model (6), by performing linear regression between experimental values of $\sqrt{-\log(\Gamma_u(\eta))}$ and η in the range of St around each peak, as illustrated in Figure 10b. Since the point $\Gamma_u(\eta = 0) = 1$ is known by construction, this reduces to evaluate one single regression coefficient a such that:

$$\sqrt{-\log(\Gamma_u(\eta))} = a\eta. \qquad (10)$$

The Gaussian coherence length is obtained afterwards by, see (6):

$$\Lambda_G = \frac{\sqrt{\pi}}{2a}. \qquad (11)$$

In the same way, *the data* is fitted to a Laplacian distribution (9) through linear regression between $-\log(\Gamma_u(\eta))$ and η, see Figure 10c, with a single regression coefficient β such that:

$$-\log\left(\Gamma_u(\eta)\right) = \beta\eta. \tag{12}$$

This yields the Laplacian coherence length as:

$$\Lambda_L = \frac{1}{\beta}. \tag{13}$$

Note that such definitions of Λ_G and Λ_L are used in order to recover the integral length Λ when the coherence decay follows one or the other model, see (5). As straightforward as it sounds, this consistency between the aeroacoustically relevant definition of the coherence length and its value yielded by the Gaussian modeling of the coherence decay or by the lag for a given coherence drop off is a definite contribution of the present paper. However, the regression of a given data-set will generally return $\Lambda_G \neq \Lambda_L$ because one model just does not work and leads to a bad fit.

For all of the 75 detected peaks, the regression is conducted for both models for each Strouhal number bin in the uncertainty interval defined in Section 3.3.1. The appropriate model if any is decided visually using plots of the linear regression and decay models compared to *the data* as illustrated in Figure 10. The adjusted determination coefficient R_a^2 objectivizes the model quality, but it is not an absolute quantificator of it. It is thus not used to select the peak Strouhal number of the model, noted St_m, which can be different from St_p, because the decay model can fit *the data* better at other frequencies without leading to a peak of coherence length. However, the raw maximum value of Λ_G or Λ_L over the Strouhal number range may also results from a biased regression: the most common example is when the Gaussian model would be good for short lags, typically up to Λ_I, while the aforementioned excess of coherence for larger lags is bending the modeled coherence length to overestimated values. Again, this is decided visually by comparing regression results for three data subsets, defined as $\eta \leq \eta_{max}$, where $\eta_{max} = \eta_{\lim}$ (default), Λ_I or $\Lambda_I/2$. Grossly, the default is generally good for the Laplacian model, while the two others apply for the Gaussian model, as exemplified in Figure 10 in the case of the two first peaks: at $St = 0.250$ (drag peak), although the Laplacian model leads to $R_a^2 = 0.92$, it is not selected for tabulation because of the poor fit for short lags obtained on chart (a). Neither is the Gaussian, which needs to exclude data for $\eta > \eta_{max} = \Lambda_I/2 \approx 1.6$ to reach $R_a^2 = 0.85$ only, resulting likely from combination of model failure and experimental bias. For the sake of completeness, all of this information (R_a^2, η_{max} and St_m) is reported in addition to either Λ_G or Λ_L, in the Supplementary file. Moreover, the best regression plot for each peak is given there too. When no model seems appropriate, only Λ_I is tabulated, for it is still valuable from the aeroacoustic point of view. Model plots for other cases are provided in Figure B.2 through literature review of coherence data and in the Supplementary file. A hybrid model [40], based on the convolution of a Gaussian and a Laplacian, may be able to correctly account for a regular behaviour at short lags and a slower decay at intermediate lags, for instance Seo and Moon's data [24] at the second peak, see Fig. B.2f).

In summary, the refined, modelled (regression induced) coherence length corresponds to a maximum over the Strouhal number range around the peak, under the strong constraint that the regression be faithful to *the data* after considering the latter's bias.

3.3.3 Influence of case and measurement method

The coherence length values at peaks, estimated as described in the previous section, are gathered in Figure 11, making more visible the influence of Reynolds number, shape and methodology: along with present data including different probe positions and velocities, literature data from experimental and numerical work is included. As discussed in Appendix B, digitization of published coherence data has allowed fair extraction of coherence length value according to present definitions of Λ_I, Λ_G and Λ_L, given in Tables B.1–B.5. If Λ_G or Λ_L is tabulated (in the Supplementary file or in Appendix B), then it is plotted, or else Λ_I is used. Recall that their definitions are such that same coherence length value means same acoustic contribution even if the coherence distribution for increasing lag is different.

For the circular cylinder at the (lift) peak, all of the experimental data agree around $\Lambda_G = 4.7$ for $10{,}000 \leq Re \leq 90{,}000$, with a very little decrease from 5.0 to 4.4 when the Reynolds number is increased. Present values are slightly below those from other works, but this can partly be associated with the regression procedure, since the agreement of *the data* is perfect, in particular at short lags, as shown in Figures 4a and B.2a–B.2c. This is also likely associated with end-condition in the present setup (no end-plates). Jacob *et al.* [13] actually investigated a rod-airfoil configuration, however it is noteworthy that the coherence length measured at the rod wall is not significantly modified by the airfoil in the wake: the value is almost the same as reported by Casalino & Jacob [5] for the isolated cylinder configuration. As already mentioned in Section 2.2, the measurement technique (wall pressure *vs.* anemometry) seems to have only a very minor influence on the coherence length value. So does the peripheral angle of the wall pressure sensor between 40° and 140°, which leads to the very narrow bounding of Maryami *et al.*'s value (however, the coherence length drops down when the sensor is at the rear or front stagnation points). Numerical simulations [24, 25, 41] have been conducted for $40{,}000 \leq Re \leq 90{,}000$ leading to dispersion from the available experimental data [13, 17], as presented in Appendix B.3. Further increasing the Reynolds number, the data reported by Fujita [6] exhibit a strong increase of the coherence length at the drag crisis, followed by $\Lambda \approx 1.8$ in the critical regime. The empirical function proposed by Norberg [12] for the one-sided spanwise correlation length models fairly well the evolution of the coherence length at the main peaks. Beyond that further consistency between the various source
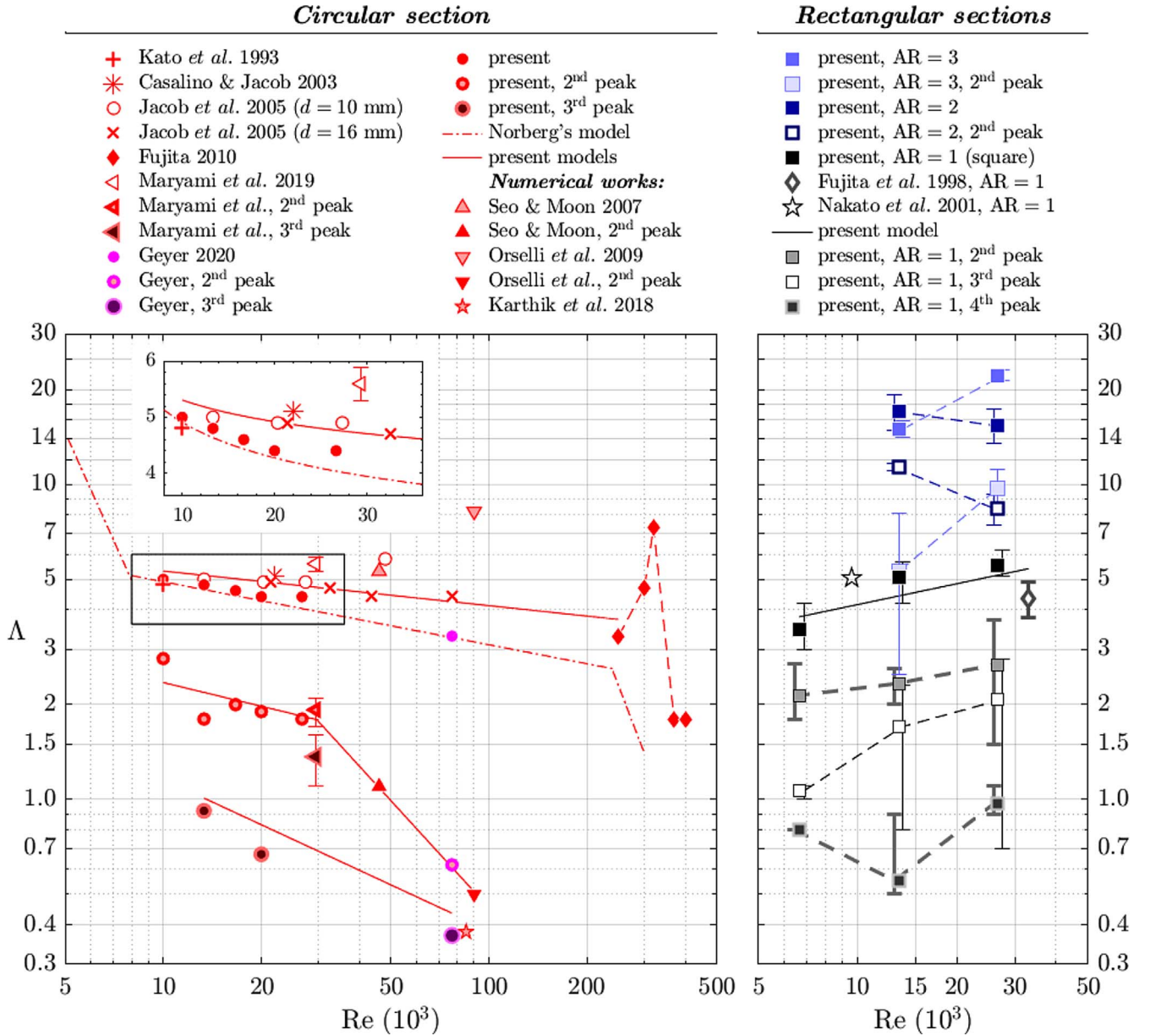
Fig. 11. Spanwise coherence length according to definition (2) in flows around circular and rectangular cylinders, at first (lift) peak unless otherwise stated. Uncertainty bars cover several probe locations. If so, the symbol is at the mean. Dashed lines for visual aid only.

of data, this means that most of the energy of the coherence spectrum is brought by the lift peak. Fitting the experimental values reported in Figure 11 with a power law leads to the following empirical model:

$$10^4 \leq \text{Re} \leq 2.5 \times 10^5, \quad \Lambda(f_0) \approx 5.31 \left(\frac{\text{Re}}{10^4} \right)^{-0.11}, \quad (14)$$

where f_0 stands for the lift peak frequency. This is a slightly weaker decay with increasing Reynolds number than Norberg's.

At the second (drag) peak, a very good agreement is noticed with the only available, experimental, literature value around 1.9 given by Maryami et al. [14]. In present results, this value is also noticed at the slower regimes,

except at Re = 10,000 where $\Lambda_{\text{L}} = 2.8$. The present coherence decays at this peak are well modeled by a Laplacian (adjusted determination coefficient $R_a^2 \geq 0.91$), and this is not contradicted by Maryami et al.'s data, as plotted in Fig. 14f). The following two-step model is found consistent with both experimental and numerical works:

$$10^4 \leq \text{Re} \leq 3 \times 10^4, \quad \Lambda(f_1) \approx 2.35 \left(\frac{\text{Re}}{10^4} \right)^{-0.25}, \quad (15)$$

$$3 \times 10^4 \leq \text{Re} \leq 9 \times 10^4, \quad \Lambda(f_1) \approx 1.81 \left(\frac{\text{Re}}{3 \times 10^4} \right)^{-1.13},$$

where f_1 stands for the drag peak frequency.

A third peak emerges for some velocities, then leading to $\Lambda_L \approx 0.8$. This is below the value reported by Maryami *et al.*, but at another regime. A power law can still be educed up to the regime tested by Geyer [17]:

$$13{,}000 \leq \text{Re} \leq 77{,}000, \quad \Lambda(3f_0) \approx 1.01 \left(\frac{\text{Re}}{13{,}000}\right)^{-0.48}. \quad (16)$$

For the square cylinder, the coherence length value at the lift peak is slightly above 5 and that of the circular cylinder for Re around 20,000, increasing from 3.5 at Re = 6,700. The Gaussian model fits well *the data* ($R_a^2 \geq 0.94$) except when the hotwire probe is in the wake (P_1). The four measurement positions in the transverse plane allows to include error bars of 20–30% in Figure 11, enabling fair comparisons with available or subsequent estimations for the same cases, for instance Fujita *et al* [23] at Re = 33,000 and Nakato *et al.* [16] at Re = 9,600 (see Appendix B.2 for a discussion of these literature values). These three data-sets can be grossly modeled as:

$$6{,}700 \leq \text{Re} \leq 33{,}000, \quad \Lambda(f_0) \approx 3.8 \left(\frac{\text{Re}}{6{,}700}\right)^{0.22}. \quad (17)$$

As mentioned in previous sections, the flow over the square cylinder exhibit more harmonics in the coherence spectrum. Up to four peaks are noted in the three tested regimes. The third peak is always visible, except for P_1 at $U_\infty = 10$ m/s. At that probe location and that velocity, the coherence length of that peak is systematically smaller than at the others (see Fig. 2 and Tab. 4 in the Supplementary file). This is likely due to the probe position in the wake, where the imprint of the shear layer flapping is weaker than that of the vortex shedding, which generates drag fluctuation, whose third peak is not an harmonic. The fourth peak is indeed well visible again there (see Tab. 5 in the Supplementary file), except at the highest velocity. However, it does not emerge from Λ_I spectrum for P_2 at Re = 6,700 and Re = 13,000 nor for P_4 at the lowest regime. This may be explained by the low value of the coherence length for that peak, approaching the shortest measured lag. It is striking indeed that for all of the harmonics, the coherence length increases with the Reynolds number. The coherence decays follows a Laplacian model for 13 peaks out of the 31 detected ones, while a Gaussian model fits the data fairly for 3 peaks, always at the slowest regime (Re = 6,700).

For rectangular cylinders, the spanwise coherence length at the main peak is very high, as commented along with Figure 7. When normalized by the cylinder span ℓ, a good agreement is obtained with Nakato *et al.*'s coherence data [16] for the case AR = 3, as plotted in Fig. B.2h). This leads to a range of L from $\ell/5$ to $\ell/4$. Since the coherence length scales better with the span than with the diameter, the flow is mostly driven by end effects, meaning that the transition to the 3D regime is not complete, or that the peak is still due to a 2D dynamics. This is also suggested by the relative sharpness of the peaks for those configurations, visible in Figure 7. This is consistent with a higher Reynolds number at the onset of unsteadiness when the aspect ratio of a given shape is increased [42]. As for the harmonics, still larger coherence lengths are noticed than that at the lift peak for circular or square shape, though with more dispersion between P_2 and P_4 at $U_\infty = 20$ m/s. The evolution with the Reynolds number is similar to that of the main peak for both geometries.

Recall that for AR = 2, the second peak is at St = 0.14, which is not twice the first peak frequency (0.08). Moreover, even if the Gaussian model would be fair at short lags (namely, up to $L_I/2$) and the Laplacian model for long lags, none of them is satisfying for the whole decay. For that reason, only Λ_I is reported in Figure 11. Nevertheless, for higher harmonics, the Laplacian decay fit the data fairly. Finally, for AR = 3, models work similarly as for the square shape, that is a Gaussian decay for the first (lift) peak, and a Laplacian for 4 out of 5 other tabulated peaks, see the Supplementary file.

3.3.4 Coherence length as an ingredient of acoustic efficiency

In the present work [1], the acoustic radiation of bluff body flows was also measured with microphones [38] while the 2D, laminar case was deeply investigated for numerous geometries [43]. The results show that, among the four geometries considered in the spanwise coherence study, the rectangular section of AR = 3 is the most silent in the 2D configuration and the loudest in the wind tunnel. Such difference in the shape aeroacoustic ranking is associated with the very high spanwise coherence length exhibited herein for this geometry. Should that be necessary, this confirm that the spanwise coherence length is a key ingredient of aeolian tone intensity.

Nevertheless, it is not the only one, as shown by the three following examples. Firstly, for the rectangular shape of AR = 2, the peak at St ≈ 0.145 has a coherence length twice that of circular or square cylinder flow at lift peak while it is not visible in the acoustic spectrum. This may be considered as an exception, however, because for the three other geometries, all of the coherent peaks emerge from the noise radiated in the transverse direction [38]. Next, some porous covers of a circular cylinder have been able to reduce the tone intensity while (drastically) increase the spanwise coherence of the flow with respect to the hard-wall cylinder of same outer diameter [17]. Finally, for the square cylinder at incidence [23], there seems to be no association of the Sound Pressure Level with the coherence length when the angle of attack is varied, as shown in Figure B.1. However, the drop of noise level around 13° of incidence may be an artifact due to the fixed microphone while the directivity pattern may tilt as noticed in numerical predictions [28].

A flow dynamics may be spanwise coherent but of low amplitude, and/or inefficient as a lift fluctuation generator by being far from the lifting surface, so that, in Curle's formalism, the overall acoustic generation shall be weak. Further modeling effort is necessary to improve the understanding of the influence of shape of aeolian tone level. Regarding the amplitude, the distance to the onset of

unsteadiness may be relevant [42]. As for the lift generation, investigating tailored Green's functions [44, 45] could be beneficial for shape comparison as well as effect of porous covering.

4 Conclusions

In the present paper, a measurement methodology is proposed that enables fair comparison of bluff body shapes from the spanwise dynamics point of view. The HWA removed bias coming from *a priori* positioning of the sensor, and allowed free exploration of the flow topology regardless the model. The possible influence of body shape on the two-point spanwise statistics was accounted for by a preliminary mean flow scan in the transverse plane.

Present coherence length values enrich the available corpus with new cases, in particular for rectangular shapes and harmonics. An important point is that the fixed detachment point at sharp edges does not necessarily go with a coherent flow all along the span at the tested regime, as evidenced by the square cylinder case. An all-data-in-one Figure 11 eases future applications for aeroacoustics, showing $\Lambda(\mathrm{Re})$ analogously to head loss tables or Nusselt number *versus* Re for different geometries. Such production needed to select one, aeroacoustically consistent definition of the spanwise coherence length, free from any determination by a decay model, and to provide a rational way for identifying peak Strouhal numbers and for model fitting. The key was to include large lags in order to cover the whole coherence decay in the present experiments, what allowed a first estimate through a frequency dependent, integral coherence length Λ_I. Moreover, the present harmonisation of the definitions of coherence length for Gaussian, Laplacian or arbitrary decays is such that, in the framework of Curle's analogy, they have equal integral, that is acoustic contribution, for a given value of Λ.

Except for AR = 2, the first (lift) peak exhibits a Gaussian coherence decay. The issue of which model is the more reliable for a given harmonic of a given case is open. Laplacian decays are obtained in the present measurements, but such model misses physical relevancy, becoming singular at short lags. Also, the model may not be the same everywhere in the flow, as exemplified in Figure B.2 by velocity data comparison with wall pressure data at the same regime. For harmonics, in most of the investigations, the resolution is not fine enough at short lags to evidence a smooth early decay, and/or the spanwise extent of numerical simulations is too short to include the full decay.

Finally, a noteworthy finding is the almost 2D character of the flow dynamics at the peak frequency for the rectangular sections of AR = 2 and 3, in which cases the coherence length scales with the body span for Re = 13,300 and 26,700. Testing other regimes could complete the knowledge of the transition process. More generally, numerical simulations of bluff body flows could help to understand the spanwise dynamics. However, present measurements and literature review draw the conclusion that this would need to simulate a span twice as long as the expected coherence length, in order not to be biased by the end-condition. Recall indeed that values gathered in Figure 11 correspond to half-lengths of the physical phenomenon.

Conflict of interest

Acknowledgments

Supplementary material

A supplementary pdf file has been made available for readers at https://acta-acustica.edpsciences.org/10.1051/aacus/2022061/olm. It contains:

- Integral coherence length spectra for the other velocities and probe positions, thus complementing Figures 7 and 8;
- Database of peak frequencies and coherence length values, including Strouhal number range as defined in Section 3.3.1 and model properties (regression parameter η_{max}, determination factor, St_m and model Λ) if any;
- Plots of coherence *data* and decay models for the 75 peaks.

References

1. Gonçalves da Silva Pinto W.J.: Modelling airframe noise: from aerodynamic topology to acoustic efficiency. PhD Thesis. Université de Poitiers, 2019. Available from: https://tel.archives-ouvertes.fr/tel-02507094.
2. F. Margnat, V. Ioannou, S. Laizet: A diagnostic tool for jet noise using a line-source approach and implicit large-eddy simulation data. Comptes Rendus Mécanique 346, 10 (2018) 903–918.
3. O.M. Phillips: The intensity of Aeolian tones. Journal of Fluid Mechanics 1, 6 (1956) 607–624.
4. P. Leehey, C.E. Hanson: Aeolian tones associated with resonant vibration. Journal of Sound and Vibration 13, 4 (1970) 465–483.
5. D. Casalino, M. Jacob: Prediction of aerodynamic sound from circular rods via spanwise statistical modelling. Journal of Sound and Vibration 262, 4 (2003) 815–844.
6. H. Fujita: The characteristics of the Aeolian tone radiated from two-dimensional cylinders. Fluid Dynamics Research 42, 1 (2010) 015002.
7. E. Baroudi: Measurements of two-point correlations of velocity near a circular cylinder shedding a Karman vortex street (Technical Note number 31). University of Toronto (UTIA), Institute of Aerophysics, 1960.

8. S.C. Kacker, B. Pennington, R.S. Hill: Fluctuating lift coefficient for a circular cylinder in cross flows. Journal of Mechanical Engineering Science 16, 4 (1974) 215–224.

9. J.L.D. Ribeiro: Fluctuating lift and its spanwise correlation on a circular cylinder in a smooth and in a turbulent flow: a critical review. Journal of Wind Engineering and Industrial Aerodynamics 40, 2 (1992) 179–198.

10. S. Szepessy, P.W. Bearman: Aspect ratio and end plate effects on vortex shedding from a circular cylinder. Journal of Fluid Mechanics 234 (1992) 191–217.

11. G.S. West, C.J. Apelt: Fluctuating lift and drag forces on finite lengths of a circular cylinder in the subcritical Reynolds number range. Journal of Fluids and Structures 11, 2 (1997) 135–158.

12. C. Norberg: Fluctuating lift on a circular cylinder: review and new measurements. Journal of Fluids and Structures 17, 1 (2003) 57–96.

13. M.C. Jacob, J. Boudet, D. Casalino, M. Michard: A rod-airfoil experiment as a benchmark for broadband noise modeling. Theoretical and Computational Fluid Dynamics 19, 3 (2005) 171–196.

14. R. Maryami, M. Azarpeyvand, A.A. Dehghan, A. Afshari: An experimental investigation of the surface pressure fluctuations for round cylinders. Journal of Fluids Engineering 141, 6 (2019) 171–196.

15. C. Kato, A. Iida, Y. Takano, H. Fujita, M. Ikegawa: Numerical prediction of aerodynamic noise radiated from low Mach number turbulent wake. In: AIAA Paper, 31st Aerospace Sciences Meeting. 1993.

16. S. Nakato, K. Kimura, Y. Fujino, T. Ogawa: Aerodynamic sound from rectangular cylinders at incidence. Journal of Wind Engineering 89 (2001) 133–136.

17. T.F. Geyer: Experimental evaluation of cylinder vortex shedding noise reduction using porous material. Experiments in Fluids 61, 7 (2020) 153–173.

18. M. Matsumoto, H. Shirato, K. Araki, T. Haramura, T. Hashimoto: Spanwise coherence characteristics of surface pressure field on 2-D bluff bodies. Journal of Wind Engineering and Industrial Aerodynamics 91, 1 (2003) 155–163.

19. T.H. Le, Y. Tamura, M. Matsumoto: Spanwise pressure coherence on prisms using wavelet transform and spectral proper orthogonal decomposition based tools. Journal of Wind Engineering and Industrial Aerodynamics 99, 4 (2011) 499–508.

20. Y. Ito, H. Shirato, M. Matsumoto: Coherence characteristics of fluctuating lift forces for rectangular shape with various fairing decks. Journal of Wind Engineering and Industrial Aerodynamics 135 (2014) 34–45.

21. L. Bruno, M.V. Salvetti, F. Ricciardelli: Benchmark on the aerodynamics of a rectangular 5:1 Cylinder: An overview after the first four years of activity. Journal of Wind Engineering and Industrial Aerodynamics 126, 87 (2014) 106.

22. L. Bruno, N. Coste, D. Fransos: Simulated flow around a rectangular 5:1 cylinder: Spanwise discretisation effects and emerging flow features. Journal of Wind Engineering and Industrial Aerodynamics. 104–106 (2012) 203–215.

23. H. Fujita, W. Sha, H. Furutani, H. Suzuki: Experimental investigations and prediction of aerodynamic sound generated from square cylinders. In: 4th AIAA/CEAS aeroacoustics conference, AIAA Paper 1998–2369. 1998.

24. J.H. Seo, Y.J. Moon: Aerodynamic noise prediction for long-span bodies. Journal of Sound and Vibration 306, 32 (2007) 564–579.

25. R. Orselli, J. Meneghini, F. Saltara: Two and three-dimensional simulation of sound generated by flow around a circular cylinder. In: 15th AIAA/CEAS Aeroacoustics Conference (Aeroacoustics 2019), AIAA Paper 2009–3270. 2009.

26. A. Rokugou, T. Kiwata, A. Okajima, S. Kimura, H. Yamamoto: Numerical analysis of aerodynamic sound radiated from rectangular cylinder. Journal of Wind Engineering and Industrial Aerodynamics 96, 10 (2008) 2203–2216.

27. C.J. Doolan: Computational bluff body aerodynamic noise prediction using a statistical approach. Applied Acoustics 71, 12 (2010) 1194–1203.

28. F. Margnat: Hybrid prediction of the aerodynamic noise radiated by a rectangular cylinder at incidence. Computers & Fluids 109 (2015) 13–26.

29. W.J.G. da Silva Pinto, F. Margnat: A shape optimization procedure for cylinders Aeolian tone. Computers and Fluids 182 (2019) 37–51.

30. W.J.G. da Silva Pinto, F. Margnat: Shape optimization for the noise induced by the flow over compact bluff bodies. Computers & Fluids 198 (2020) 104400.

31. H. Bai, Z. Lu, R. Wei, Y. Yang, Y. Liu: Noise reduction of sinusoidal wavy cylinder in subcritical flow regime. Physics of Fluids 33, 10 (2021) 105120.

32. W.G. Pinto, F. Margnat, C. Noûs: Experimental study of the influence of the shape on the spanwise coherence length of the flow over a bluff body. In: Forum Acusticum, Lyon, France. 2020, pp. 1515–1522.

33. W.J. Pinto, F. Margnat, C. Noûs, Influence of the length of a cylinder on its Aeolian Tone Level: Measurement and modelling. In: 14th WCCM-ECCOMAS Congress, Paris, France, Vol. 1500. 2021.

34. B. Ahlborn: The clockwork of vortex shedding. Physics Essays 11 (1998) 144–154.

35. M. Gruber: Airfoil noise reduction by edge treatments. PhD Thesis. University of Southampton, 2012.

36. M.S. Howe: Sound generation in a fluid with rigid boundaries. Cambridge Monographs on Mechanics. Cambridge University Press, 1998, 157–252.

37. M. Abramovitz, I.A. Stegun: Handbook of mathematical functions. With formulas, graphs and mathematical tables, Dover, 1964.

38. W.J.G.S. Pinto, F. Margnat, Y. Gervais: Effect of cross-section on flow three-dimensionality for prismatic bodies and the associated noise emission. In: 25th AIAA/CEAS Aeroacoustics Conference (Aeroacoustics 2019), AIAA Paper 2019–2531. Delft, The Netherlands, 2019.

39. S. Piantanida, V. Jaunet, J. Huber, W.R. Wolf, P. Jordan, A.V. Cavalieri: Scattering of turbulent-jet wavepackets by a swept trailing edge. The Journal of the Acoustical Society of America 140, 6 (2016) 4350–4359.

40. I.A. Maia, P. Jordan, A.V.G. Cavalieri, V. Jaunet: Two-point wavepacket modelling of jet noise. Proceedings of the Royal Society A 475, 2227 (2019) 20190199.

41. K. Karthik, S. Vengadesan, S.K. Bhattacharyya: Prediction of flow induced sound generated by cross flow past finite length circular cylinders. The Journal of the Acoustical Society of America 143, 1 (2018) 260–270.

42. W.J.G.S. Pinto, F. Margnat: Influence of cylinder breadth and shape on the onset of flow unsteadiness and the Aeolian tone level. Computers & Fluids 228 (2021) 105067.

43. W.J.G.S. Pinto, F. Margnat, Y. Gervais: Influence of cross-section on the Aeolian tone: a numerical study in the laminar regime. In: 25th AIAA/CEAS Aeroacoustics Conference (Aeroacoustics 2019), AIAA Paper 2019–2532, Delft, The Netherlands. 2019.

44. M.S. Howe: Theory of vortex sound. Cambridge University Press, 2003.

45. X. Gloerfelt, F. Pérot, C. Bailly, D. Juvé: Flow-induced cylinder noise formulated as a diffraction problem for low Mach numbers. Journal of Sound and Vibration 287, 1–2 (2005) 129–151.

46. A. Rohatgi: Webplotdigitizer: Version 4.5. 2021. Available from: https://automeris.io/WebPlotDigitizer.

Appendix A

HWA probe positions for the spanwise study

The coordinate system starts at the center of the downstream face of the cylinder's cross-section (see Fig. 2). Spanwise measurements at P_1, fixed at $(x, y) = (1.0d, 0)$ for all velocities, and P_3 are used with the square section only. For the circular cylinder, all measurements are performed at $(x, y) = (0, 0.9d)$. The other positions follow the topology of the mean flow, as presented in Section 2.3.1, and are given in Table A.1.

Appendix B

B Review of literature data

In this section, the literature material used in Figure 11 is reviewed, starting by measurements before considering numerical simulations. Charts showing coherence data and model curves were digitized online using WebPlotDigitizer [46] in order to estimate coherence length values for present definition. This allowed direct data comparison for given shape, regime and peak, as plotted in Figures 4 and B.2. In the following discussion, *Figure* N, *equation* M and *sec.* L refer to figure, equation and section numbers in the cited work, respectively. Literature excerpts are in italic.

B.1 Experimental data for the circular cylinder

B.1.1 Measurements in Japan

The Japanese study by Kato *et al.* [15] has been pioneering in addressing the spanwise problem for cylinder computational aeroacoustics, laying the foundations of correction methods, which use spanwise coherence length to adapt numerical simulation of a short cylinder in view of comparison with experiments over a longer one. A 10 mm diameter circular cylinder was placed in an air flow at 15 m/s. The details of the experiment was to "*be published elsewhere*", but to the best of our search we could not find that dedicated paper. Therefore, it is not clear to us whether the experimental values for the coherence function shown in *Figure 10* for comparison purpose are from surface pressure or velocity field. Indeed, in a footnote page 4, the coherence function is clearly related to surface pressures, while the only measurement method mentioned in the paper is the hot-wire anemometer (see comment above *Fig. 8*). Anyway, after digitizing *Figure 10* data, a very good agreement is noticed with present's in Fig. B.2a). Regressing it with a Gaussian model, we obtained $\Lambda_G \approx 4.8$, with an adjusted determination coefficient of 0.99, for that Re = 10,000 flow. This is reported in Table B.1.

These Authors introduced the coherence length "*as the spanwise spacing where coherence function of the surface pressure drops to a critical value of one half [which] was*

Table A.1. Measurement coordinates in the XY plane.

AR	P_2	P_3	P_4
	Re = 6,667 (U_∞ = 10 m/s)		
1.0	$(-0.6d, 0.8d)$	$(0.1d, 0.9d)$	$(0.4d, 0.9d)$
	Re = 13,333 (U_∞ = 20 m/s)		
1.0	$(-0.8d, 0.8d)$	$(-0.1d, 1.0d)$	$(0.5d, 1.1d)$
2.0	$(-0.8d, 1.2d)$	$(1.1d, 1.4d)$	$(2.6d, 1.6d)$
3.0	$(-2.2d, 1.1d)$	$(-0.3d, 1.2d)$	$(0.6d, 1.4d)$
	Re = 26,667 (U_∞ = 40 m/s)		
1.0	$(-1.0d, 0.7d)$	$(-1.0d, 1.1d)$	$(0.5d, 1.2d)$
2.0	$(-1.2d, 1.2d)$	$(0.6d, 1.4d)$	$(2.1d, 1.7d)$
3.0	$(-2.2d, 1.2d)$	$(-1.3d, 1.3d)$	$(-1.0d, 1.4d)$
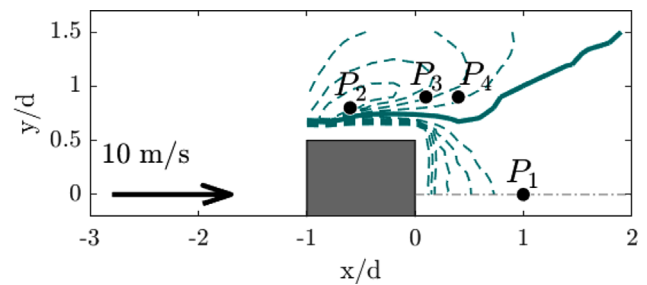
Fig. A.1. Mean flow over a rectangular cylinder of AR = 1 (square cylinder) Re = 6,700. Isocontours of velocity norm from 0.4 U_∞ to 1.6 U_∞ by step of 0.1 U_∞. The full, thick line is where $U = U_\infty$. The labeled bullets (•) are the position of the probes in the spanwise study.

determined rather ad hoc." (last paragraphs before the Results section in [15]). The agreement is noteworthy between that pioneering coherence decay value of 0.5 with that obtained here using a Gaussian model and a definition based on acoustic efficiency ($\exp(-\pi/4) \approx 0.46$, see Sect. 3.2.1).

Wall pressure measurements at higher Reynolds numbers were reported by Fujita [6] (*Fig. 23*) and "*the estimation of [coherence] length was attempted by calculating the integral scale using the Gaussian distribution curve fitting.*" Reference to Phillips [3], who provided an integral definition in *equation* (2.6), is made by Fujita [6] when defining the *correlation length* before *equation* (7), thus it is likely that the Author used the same definition as us. As a matter of fact, after digitizing some of *Figure 23* data, for those that are well fitted by a Gaussian decay, we obtain exactly the same values as those plotted in *Figure 24* for pressure transducers located at 90° and reported here in Table B.1. At other Reynolds numbers, the Gaussian model seems less accurate, while additional values of Λ_I could be extracted from *Figure 23*. A maximum of coherence length is noticed just before the critical regime.

B.1.2 Wall pressure measurements at Lyon, France

Coherence between spanwise distributed wall pressure sensors was measured about 20 years ago in the anechoic

Table B.1. Coherence length at the main peak, from Japanese studies [6, 15]. Λ is computed from integration or regression of data from *Figure 10* [15] and *Figure 23* [6], partly reproduced in Figures B.2a and B.2e.

Reference	d (mm)	Re	Λ_I	Λ_G	Λ_L
Kato *et al.* [15]	10	10,000		4.8	
Fujita [6]	267	250,000		3.3	
		300,000		4.7	
		320,000			7.3
		370,000	1.8		
		400,000		1.8	

Table B.2. Coherence length values extracted from measurements at Lyon, France [5, 13]. Λ_G is read in *Figure 4a* [5] and *Figure 7* [13] on the lag axis where the Gaussian lines reach $-\pi/4 \approx -0.785$ and $\exp(-\pi/2) \approx 0.208$, respectively. Λ_G^* is obtained by present fitting (10) of the original coherence data.

Reference	d (mm)	U_∞	Re	Λ_G	Λ_G^*
Casalino & Jacob [5]	16	20.0	22,000	5.1	4.4
Jacob *et al.* [13]	10	20.0	13,300	5.0	5.1
		30.5	20,300	4.9	5.0
		41.0	27,300	4.9	4.8
		72.0	48,000	5.8	5.4
	16	20.0	21,300	4.9	4.5
		30.5	32,500	4.7	4.3
		41.0	43,700	4.4	4.0
		72.0	76,800	4.4	4.0

wind tunnel of the Ecole Centrale de Lyon in the framework of a project funded by the European Union. Both coherence data and values of coherence length were documented [5, 13]. For the flow at $U_\infty = 20$ m/s over a 16 mm diameter circular cylinder, at the peak frequency, "*data are fitted by a Gaussian $\exp(-\eta^2/2L_g^2)$ function, with $L_g = 4.7$ for the coherence function*", as Casalino and Jacob reported (see *Sect.* 3.2 in [5]). However, such definition yields $\mathrm{Log}\Gamma = -0.5$ for $\eta = L_g$. Now, considering *Figure 4a* in [5], where $\log\Gamma$ is plotted *vs.* η, the Gaussian model reaches the value -0.5 when $\eta \approx 3.9$. Moreover, for the same cylinder flow (though with an airfoil placed 6 diameters downstream), Jacob *et al.* reported $L_g = 5.8d$ in the inner legend of *Figure 7* (bottom) in [13], with no explicit definition for L_g except a reference to [5].

In that second paper [13], the charts give Γ^2 vs. η, meaning that where the Gaussian model reaches $\Gamma^2 = e^{-1} \approx 0.37$ one could graphically read $L_g \approx 4.0$ on the η axis, consistently with the value obtained from the first paper [5]. Recall finally that present coherence data agree well with both reported measurements, as shown in Figures 4 (left) and B.2b–B.2c. Thus, a typo seems likely at the link between the definition of L_g and the regression coefficient. In order to enable comparison with present values, coherence length for both these studies is obtained graphically from the Gaussian lines in *Figure 4a* [5] and *Figure 7* [13], as the lag where the plotted quantity reaches the value issued from present definition (6), that is $-\pi/4 \approx -0.785$ for $\log\Gamma_G$ and $\exp(-\pi/2) \approx 0.208$ for Γ_G^2, respectively. The extracted values are listed in Table B.2, plotted in Figure 11 and discussed in Section 3.3.3.

When both datasets are fitted in the present way (10), similar values of Λ_G with the Authors' are obtained at the 3 lowest flow velocities for the $d = 10$ mm cylinder, see Table B.2. The discrepancies can fairly be attributed to round-offs or digitization. However, for the highest velocity or for the $d = 16$ mm cylinder, little excess of coherence is noticed at the two largest lags in Figures B.2c–B.2e, possibly associated with the smaller span to diameter ratio. Removing those lags from the fitting procedure yields 10% lower values of Λ_G^* reported in Table B.2 for the corresponding cases, in still better agreement with present measurements. However, considering it is safer to document higher Λ, original Λ_G values are left in Figure 11, more faithfully to the Authors' analysis.

B.1.3 Other studies

The study by Maryami *et al.* [14] has been the only experimental work reporting wall pressure coherence data for several angular positions (θ) around the cylinder and for harmonics. In *Figure 11*, Γ_p^2 is plotted *vs.* the spanwise lag for the first three peaks, namely St ≈ 0.2, 0.4 and 0.6, and fitted with Gaussian models. Very low coherence level is noted at the stagnation points, except for the drag peak at the rear one ($\theta = 180°$). For $\theta = 45°$, $90°$ and $135°$, the data is similar. At the fundamental frequency, a coherence length value following the present definition can be obtained graphically from the Gaussian lines in *Figure 11a* [14] as the lag where Γ_p^2 reaches $\exp(-\pi/2) \approx 0.208$. The extracted values are listed in Table B.3. This experimental setup being very similar to that in Lyon, fitting the data with more weight on the short lags leads to lower Gaussian coherence length Λ_G^* here also. At the harmonics, the Gaussian model hardly fits the data. A frequency dependent coherence length is also provided in *Figure 12*, defined in *equation (2)* as the infinite integral of the root-coherence over positive lags, showing a value of e.g. ≈ 8 at the main peak. This is inconsistent with the data plotted in *Figure 11*, whose $\Lambda_G \approx 5.3$ is indeed the quadrature value, given present definitions. The same appear for the other peaks, by comparing *Figure 12* with trapezoidal rule of the Authors' data (after rooting it to get Γ) reported in Table B.3.

Coherence data was also reported by Geyer [17], who conducted aeroacoustic tests for circular cylinders with porous covers. Thanks to courtesy share by this Author, the methodology described in Section 3 could be applied to his data, which was obtained by HWA, the probes being placed one diameter downstream of the body, on the symmetry axis (this would correspond to P_1 in the present study). The obtained values for St$_p$ and Λ_I are listed in Table B.4 for the three peaks that emerge from the coherence spectra. For the harmonics, too few data points are involved at such short lag, and no regression could be fairly conducted. At the main peak, however, *the data*, in spite of high variance, is better fitted by a Laplacian decay, as plotted in Fig. B.2e), leading to $\Lambda_L = 3.3$. This value is 25%

Table B.3. Coherence length values for the circular cylinder flow at Re = 30,000, extracted from Maryami *et al.* [27]. Λ_G is read in *Figure 11a* on the lag axis where the Gaussian lines reach $\exp(-\pi/2) \approx 0.208$. Λ_I is computed by trapezoidal integration of the square root of data from *Figure 11*. Λ_G^* is obtained by present fitting (10) of the original coherence data.

Angular position (θ)	45°	90°	135°	180° (rear)
1st peak, Λ_G	5.9	5.3	5.6	
1st peak, Λ_G^*	4.9	4.0	4.2	
2nd peak, Λ_I	2.1	1.7	1.8	2.1
3rd peak, Λ_I	1.6	1.4	1.1	

Table B.4. Coherence length values for the circular cylinder flow at Re = 77,000, computed from *the data* reported by Geyer [17].

1st peak	St_p	0.173 (0.161–0.200)
	Λ_I	2.8
	Λ_L (R_a^2)	3.3 (0.79)
	St_m	0.173
2nd peak	St_p	0.336 (0.312–0.343)
	Λ_I	0.62
3rd peak	St_p	0.552 (0.536–0.555)
	Λ_I	0.37

smaller than that reported by Jacob *et al.* [13] at the same regime (Re = 77,000). The regression may have favored large lags in that latter study, as visible in Fig. B.2e), leading to overestimation of Λ_G, but the difference may rather be associated with the measurement techniques: in Lyon, coherence data was obtained from wall pressure at $\theta = 90°$. Now, as shown by Maryami *et al.* [14], the wall pressure coherence level is smaller at the rear of the body. Moreover, a Laplacian decay is evident at the drag peak in present data plotted in Fig. B.2f), while no Gaussian model was found fair at P_1 in the case of the square cylinder (see Table 2 and Figures 6, 10 and 14 in the Supplementary file). This leads to the conclusion that placing the velocity probe on the wake axis in the drag generation region could explain both the lower coherence length value and the different decay type at the lift peak. Moreover, both effects may be stronger as the Reynolds number increases.
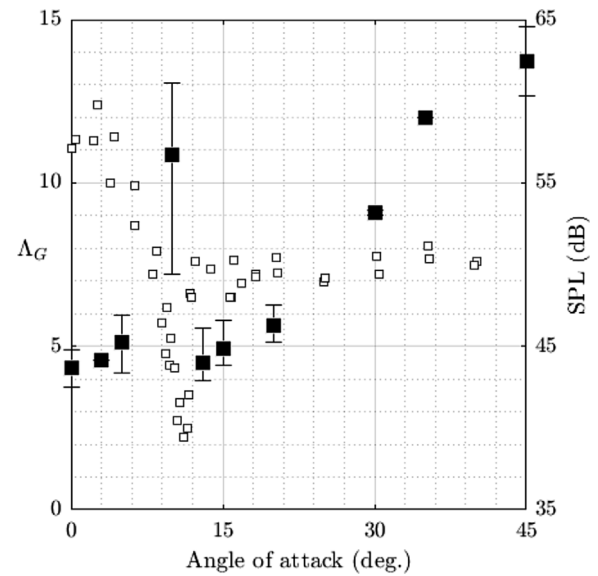
B.2 Experimental data for rectangular cylinders

The spanwise coherence in the square cylinder flow at 25 m/s was measured by Fujita *et al.* [23] using 20 equally-spaced pressure transducers over the 200 mm span of the 20 mm side body (Re = 33,000). The effect of the flow angle of attack (AoA) on the aeolian tone properties was investigated. Coherence data are reported in *Figure 8* for several AoA, but not for the flow-parallel case. However, values of the normalized coherence length are plotted in *Figure 9* for $0 < \mathrm{AoA} \leq 180°$. These Authors used an integral scale of the coherence function as a definition. Namely, Gaussian model coefficients given in *Figure 8* lead to values in *Figure 9* by taking $\sqrt{\pi/\alpha}$, see (4) and (5). Thus, present definition is recovered by halving these Authors' values, as plotted in Figure B.1, and the value for the flow without incidence is obtained from that at AoA of 90° and 180°. This is the same flow indeed, even if the monitored square side is different. That is why those values are considered here as two estimations of the same quantity, just like it is done in the present study for the four probe locations. Cases of AoA larger than 45° come down to the range 0–45°, yielding uncertainty ranges similarly.

Contemporaneously with the above cited Japanese studies, Nakato *et al.* [16] reported coherence data at the peak frequency for flows over a square cylinder and a rectangular cylinder with AR = 3, at Re $\approx$ 9,600. The Authors used HWA with the probes placed one cylinder breath


Fig. B.1. Coherence length (■ with error bars) and Sound Pressure Level (SPL, □) for a 20 mm side square cylinder at incidence in a flow at 25 m/s, according to Fujita *et al.* [23]. Note that the coherence length is given as normalized by the square side, which does not correspond with the body height at incidence (referred to as "the effective geometrical width normal to the flow" by the Authors).

downstream of the cylinder back. For the square cylinder flow, this corresponds to P_1 in the present study, and the data have been compared in Figure 4 (right). Trapezoidal integration of the Authors' data above $\Gamma = 0.2$ yields $\Lambda_I \approx 5.0$. This is slightly below the value 5.7 obtained here at P_1 for Re = 13,300 (see Tab. 2 in the Supplementary file). The present overestimation can be associated with excess coherence for $\eta \geq 7$ in the present case (see Fig. 4, right), while such end-effect may not appear in [16] where a very long span (180 diameters) was combined with end plates. Those estimations of $\Lambda \approx 4.5$ by Fujita *et al.* [23] from wall-pressure measurements and by Nakato *et al.* [16] from HWA, in agreement with present data, shows that a sharp-edge geometry does not necessarily leads to a higher spanwise coherence length than a smooth geometry for $9,700 \leq \mathrm{Re} \leq 33,000$.
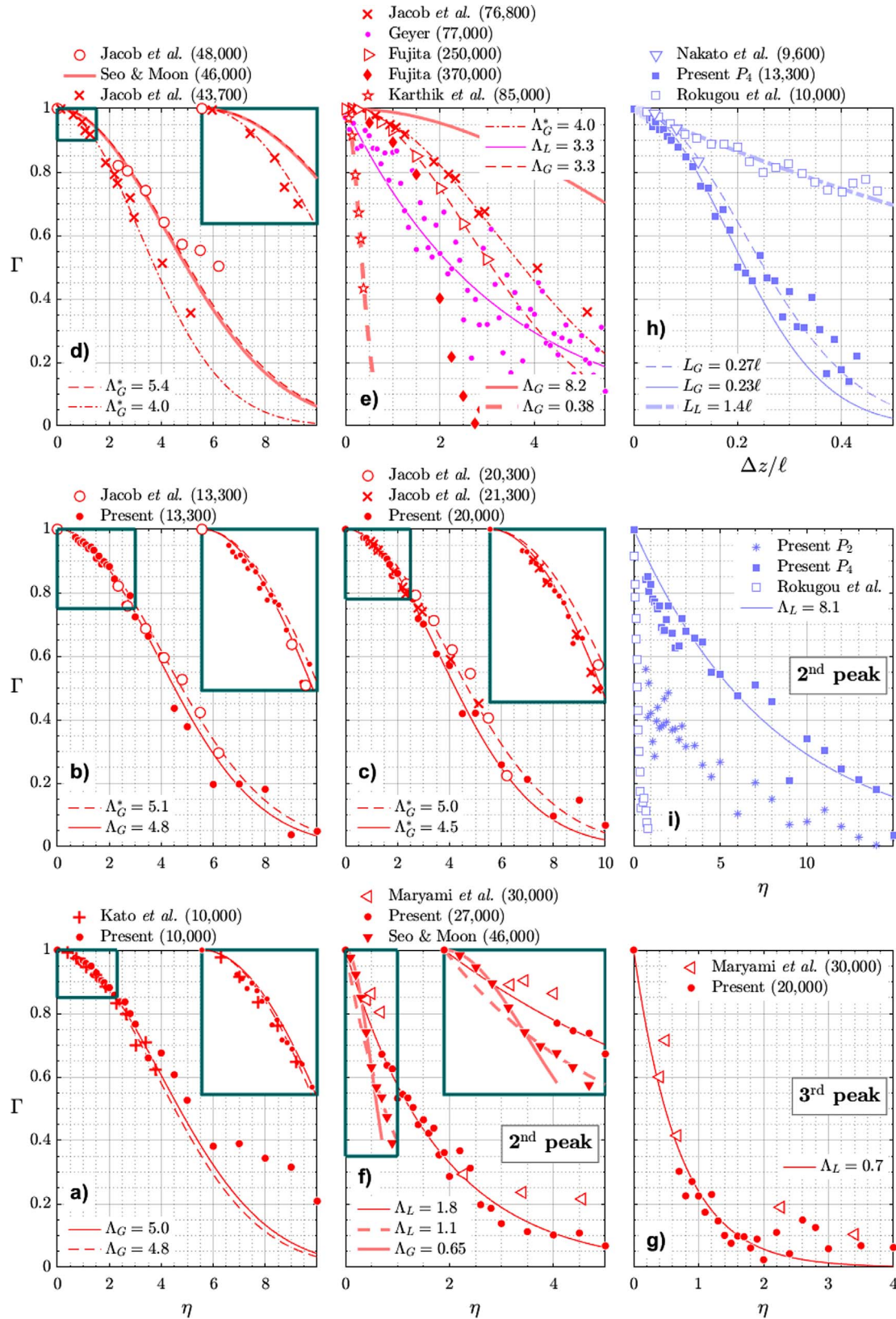
Fig. B.2. Spanwise coherence data (symbols) and model (lines) for the flow over a circular (a–g) and a rectangular of AR = 3 cylinder (h, i). Literature data and models have been obtained as described in Appendix B. Data from Maryami et al. [14] are for $\theta = 135°$. In (e), the line $\Lambda_G = 8.2$ accounts for the numerical data reported by Orselli et al. [25] (Re = 90,000). The Reynolds numbers in (i) are the same as in (h).

Table B.5. Numerical studies reporting spanwise coherence data of cylinder flows in the framework of aeroacoustics. For rectangular (rect) cross-sections, the parenthesized numbers are the breadth (b) to height (d) ratio, denoted as AR $= b/d$ herein.

Reference		Reynolds number	Cross-section	ℓ/d	Boundary Condition	1st peak	2nd peak
Rokugou *et al.* (2008)	[26]	10,000	Rect (0.6)	8.0	Periodic	$\Lambda_G = 3.2$	$\Lambda_I = 0.4$
			Rect (3.0)			$\Lambda_L = 11.4$	$\Lambda_I = 0.2$
Seo and Moon (2007)	[24]	46,000	Circular	3.0	Periodic	$\Lambda_G = 5.3$	$\Lambda_I = 1.1$
Orselli *et al.* (2009)	[25]	90,000	Circular	2.5	Periodic	$\Lambda_G = 8.2$	$\Lambda_I = 0.5$
Karthik *et al.* (2018)	[41]	85,000	Circular	35.0	Finite cylinder	$\Lambda_G = 0.38$	

As for the rectangular cylinder with AR $= 3$, the coherence is reported for three lags: $\eta = [7.5, 15, 22.5]$. A Gaussian model fits well ($R_a^2 = 0.99$) the decay with $L_G \approx 48d$, as visible in Figure B.2h. This is consistent with the present result of a flow still in the 2D regime for the main flapping mode. Indeed, although the coherence lengths are thus of different values if normalized by the diameter, Nakato *et al.* [16] data return $L_G \approx \ell/3.8$ while present data lead to $L_G \approx \ell/5.0$ and $\ell/4.4$ for P_2 and P_4 respectively at Re $= 13{,}300$. The slightly lower coherence length, once normalized by the cylinder span, obtained in the present experiment may be associated with the end conditions: 2.5 times shorter span, and no end-plates (so that the span effectively wetted by the potential flow shall be considered a little bit shorter than the jet width of $70d$).

B.3 Numerical works

A couple of numerical studies on cylinder aeroacoustics reported spanwise coherence data, whose characteristics are summarized in Table B.5. Seo and Moon [24] proposed a correction method to compare noise prediction based on Large Eddy Simulation of the flow over a short span ($\ell = 3d$ in their case) with experimental data obtained for longer cylinders. The spanwise coherence length is a key element of such method. Coherence data for the surface pressure at $\theta = 90°$ is provided in *Figure 13* for lags up to one diameter at Re $= 46{,}000$. For the lift peak, the coherence level is still above 0.98 for the largest lag. This makes digitization of the published chart a hard task. However, the regression with a Gaussian decay provided by the Authors yields $\Lambda_G = 5.3$ in agreement with Jacob *et al.* [13]. For the drag peak, the numerical data is well fitted by a Gaussian decay with $\Lambda_G = 0.6$ for $\eta \leq 0.4$ and by a Laplacian with $\Lambda_L = 1.1$ decay beyond (see the inset in Fig. B.2f). Combining both models allows to estimate $\Lambda_I \approx 1.1$. This is consistent with, and interestingly complementing at short lags, available experimental values at this frequency. In a similar study, Orselli *et al.* [25] simulated the flow at Re $= 90{,}000$

over a 2.5 diameter long circular cylinder. The same remark holds for coherence data at the lift peak (*Fig. 11*), leading to $\Lambda_G = 8.2$. This is about twice as high than values reported by Jacob *et al.* [13] at Re $= 76{,}800$ or Fujita [6] at Re $= 250{,}000$. At the drag peak, the coherence data exhibits a plateau around $\Gamma \approx 0.5$ for $0.05 \leq \eta \leq 0.8$, yielding $\Lambda_I \approx 0.5$.

Coherence data of local fluctuations in fluid force on rectangular cylinders were reported by Rakugou *et al.* [26] from numerical simulation of a $\ell = 8d$ spanwise extended computational domain using periodic boundary condition, at Re $= 10{,}000$. The plot of coherence decays at peak frequencies is not provided for the square section, however, data for AR $= 0.6$, provided in *Figure 12*, lead to $\Lambda_G = 3.2$ and $\Lambda_I = 0.4$ for the lift and drag peaks, respectively. The first value is in good agreement with those reported in the present study for the square section at the lowest velocity. Data at the main peak for AR $= 3$ (*Fig. 14*) is well fitted by a Laplacian decay, leading to $\Lambda_L = 11.4$. This is larger than ℓ, like the coherence length reported for the main peak by the numerical studies on the circular cylinder using periodic boundary conditions. However, the level of coherence at harmonics seems underestimated by the simulations.

Different spanwise extents of the computational domain were tested by Karthik *et al.* [41] for the circular section at Re $= 85{,}000$, combined with a finite span cylinder boundary condition: the simulated domain extends $7.5d$ beyond the body span at each end. Surprisingly, no coherence data is reported in *Figure 18* for greater lags than $0.5d$ even for the $\ell = 35d$ cylinder case, and the good fit with a Gaussian model leads to $\Lambda_G = 0.4d$ at the main peak frequency.

One may conclude from Table B.5 that the accurate simulation of the spanwise coherence decay of the flow in the subcritical regime at peak frequencies is a difficult and/or expensive task, the issue of the necessary simulation time to converge coherence statistics at low frequencies notwithstanding.